

Revisiting the relation between momentum and scalar roughness lengths of urban surfaces

Article

Accepted Version

Li, Q., Bou-Zeid, E., Grimmond, S. ORCID: <https://orcid.org/0000-0002-3166-9415>, Zilitinkevich, S. and Katul, G. (2020) Revisiting the relation between momentum and scalar roughness lengths of urban surfaces. *Quarterly Journal of the Royal Meteorological Society*, 146 (732). pp. 3144-3164. ISSN 1477-870X doi: <https://doi.org/10.1002/qj.3839> Available at <https://centaur.reading.ac.uk/91220/>

It is advisable to refer to the publisher's version if you intend to cite from the work. See [Guidance on citing](#).

Published version at: <http://dx.doi.org/10.1002/qj.3839>

To link to this article DOI: <http://dx.doi.org/10.1002/qj.3839>

Publisher: Wiley

All outputs in CentAUR are protected by Intellectual Property Rights law, including copyright law. Copyright and IPR is retained by the creators or other copyright holders. Terms and conditions for use of this material are defined in the [End User Agreement](#).

www.reading.ac.uk/centaur

CentAUR

Central Archive at the University of Reading

Reading's research outputs online

1 **ORIGINAL ARTICLE**

2 **Journal Section**

3 **Revisiting the Relation Between Momentum and**
4 **Scalar Roughness Lengths of Urban Surfaces**

5 **Qi Li^{1*2} | Elie Bou-Zeid² | Sue Grimmond³ | Sergej**
Zilitinkevich⁴ | Gabriel Katul^{5,6,2}

¹School of Civil and Environmental Engineering, Ithaca, NY, USA

²Department of Civil and Environmental Engineering, Princeton, NJ, USA

³Department of Meteorology, University of Reading, Reading, UK

⁴Finnish Meteorological Institute, P.O. Box 503, 00101 Helsinki, Finland

⁵Nicholas School of the Environment, Duke University, Durham, NC, USA

⁶Department of Civil and Environmental Engineering, Duke University, Durham, NC, USA

Large Eddy Simulations (LES) of neutral flow over regular

Correspondence

Email: ql56@cornell.edu

Funding information

Support was provided by start-up funds from Cornell University; the small allocation grant for new faculty by the National Center for Atmospheric Research (NCAR), NOAA-Princeton Cooperative Institute for Climate Science (CU00029), Princeton's Andlinger Center for Energy and the Environment, and the U.S. National Science Foundation (NSF) Sustainability Research Network (Cooperative Agreement 1444758 and grant 1664091). High-performance computing support from Cheyenne (doi:10.5065/D6RX99HX) provided by NCAR's Computational and Information Systems Laboratory (NSF projects P36861020 and UPRI0007) is acknowledged. SZ acknowledges support from the Academy of Finland (grant 314 798/799), and GK acknowledges partial support from NSF-AGS-1644382 and NSF-IOS-1754893. The Metropolis Project is acknowledged for supporting the collaborative visit of GK to Princeton University.

arrays of cuboids are conducted to explore connections between momentum (z_{0m}) and scalar (z_{0s}) roughness lengths in urban environments, and how they are influenced by surface geometry. As LES resolves the obstacles but not the micro-scale boundary layers attached to them, the aforementioned roughness lengths are analyzed at two distinct spatial scales. At the micro-scale (roughness of individual facets, e.g. roofs), it is assumed that both momentum and scalar transfer are governed by accepted arguments for smooth walls that form the basis for the LES wall model. At the macro-scale, the roughness lengths are representative of the aggregate effects of momentum and scalar transfer over the resolved roughness elements of the whole surface, and hence they are directly computed from the LES. The results indicate that morphologically-based parameterizations for macro-scale z_{0m} are adequate overall. The relation between the momentum and scalar macro-roughness values, as conventionally represented by $\log(z_{0m}/z_{0s})$ and assumed to scale with Re_*^n (where Re_* is a roughness Reynolds number), is then interpreted using surface renewal theory (SRT). SRT predicts $n = 1/4$ when only Kolmogorov-scale eddies dominate the scalar exchange, whereas $n = 1/2$ is predicted when large eddies limit the renewal dynamics. The latter is found to better capture the LES results. However, both scaling relations indicate that z_{0s} decreases when z_{0m} increases for typical urban geometries and scales. This is opposite to how their relation is usually modeled for urban canopies (i.e. z_{0s}/z_{0m} is a fixed value smaller than unity).

KEYWORDS

large-eddy simulation, scalar roughness length, surface renewal theory, urban canopy

7

8 1 | INTRODUCTION

9 1.1 | Overview of roughness lengths

10 Quantification of momentum, heat, water vapor and other trace gas fluxes over built surfaces remains a first-order
11 challenge in modeling and observation of urban climates and meteorology (Masson, 2000; Grimmond and Oke, 2002;

12 Bou-Zeid et al., 2009; Llaguno-Munitxa and Bou-Zeid, 2018). Monin-Obukhov similarity theory (MOST) (Monin and
 13 Obukhov, 1954) remains the cornerstone for representing these turbulent exchanges between the earth surface and
 14 the lower atmosphere although possible refinements accounting for deviations from MOST in the roughness sublayer
 15 have been proposed for urban (Theeuwes et al., 2019) and vegetated canopies (Garratt, 1980; Harman and Finnigan,
 16 2007, 2008). The roughness lengths used in MOST are of significance in coupled urban-atmospheric models: they
 17 encapsulate how turbulent exchanges depend on the characteristics of the underlying surface such as geometric or
 18 thermal properties, and on the spatial distributions of scalar sources/sinks at the surface (Garratt, 1992). In MOST,
 19 the momentum and scalar roughness lengths (z_{0m} and z_{0s}) for neutral atmospheric flows are used to determine the
 20 surface drag (represented by the friction velocity u_*) and scalar fluxes (represented by the scalar, here temperature,
 21 scale θ_*) based on the mean profiles of streamwise velocity \bar{u} and temperature $\bar{\theta}$ via

$$u_* = \bar{u} \left[\frac{1}{\kappa} \log \left(\frac{z-d}{z_{0m}} \right) \right]^{-1} \quad (1)$$

22 and

$$\theta_* = (\bar{\theta}_s - \bar{\theta}) \left[\frac{1}{\kappa} \log \left(\frac{z-d_s}{z_{0s}} \right) \right]^{-1}, \quad (2)$$

23 where κ is the von Kármán constant (κ is assumed to be 0.4); d and d_s are the displacement heights of momentum
 24 and scalars, respectively; $\bar{\theta}_s$ is the 'aerodynamic' mean surface temperature, which is obtained by extending the scalar
 25 logarithmic profile to $z = z_{0s} + d_s$; u_* is the friction velocity; and $\theta_* = F_c/u_*$ where F_c is the kinematic surface scalar
 26 flux (here sensible heat flux).

27 Roughness lengths and corollary concepts such as friction factor have been extensively studied in both the en-
 28 gineering and the atmospheric sciences communities since the early 20th century. Rough-wall turbulent boundary
 29 layers were examined in the classic experiments by Nikuradse (1933) for turbulent flows over sand roughness cover-
 30 ing the walls of a pipe in the absence of buoyancy forces. Since then, the concept of 'roughness function' has been an
 31 active area of research in the engineering community (Perry et al., 1969; Flack and Schultz, 2014). In hydrology, the
 32 distinction between z_{0m} and z_{0s} over a variety of natural surfaces gained significant research attention with the prolif-
 33 eration of remote-sensing platforms that now will skin temperature at high spatial and temporal resolution (Schmugge
 34 et al., 2002; Morrison et al., 2020). Early analysis by Brutsaert (1975b) showed that scalar transfer differs for smooth
 35 and rough natural surfaces despite the fact that both are driven by molecular exchange. For a rough surface, it is
 36 now well established that z_{0m} and z_{0s} are not equal (Garratt, 1992, Chap.4). Similarity between turbulent transport
 37 of momentum and scalars (i.e. the Reynolds analogy) is generally valid for high Reynolds number (Re) flows (Yang and
 38 Abkar, 2018), thus justifying the existence of a logarithmic layer for a passive scalar in Eq. 2. However, inequality
 39 between z_{0m} and z_{0s} still arises because in the 'immediate vicinity' of the wall (Brutsaert, 1975a), (i.e. the interfacial
 40 sublayer between the fluid and surface of the roughness elements), the mechanisms of scalar and momentum transfer
 41 differ. While scalar transfer relies on molecular diffusion, momentum transfer is dominated at high Re by pressure (or
 42 form) drag in addition to the viscous drag (Brutsaert, 1975a,b).

43 Conventionally, z_{0s} is related to z_{0m} using the quantity $\kappa B^{-1} = \log(z_{0m}/z_{0s})$ (Owen and Thomson, 1963; Garratt,
 44 1992) because of the large variations expected in z_{0m}/z_{0s} . Although it is less discussed in the literature, d and d_s may
 45 also be unequal if momentum sinks and scalar sources/sinks drastically differ when eddy penetration into roughness
 46 elements is incomplete (Siqueira and Katul, 2010). Finally, roughness length concepts extend beyond the framework
 47 of MOST. Roughness lengths are indispensable model parameters when using the aerodynamic resistance approach

48 (ARM), which is ubiquitously applied in various subfields of meteorology (Lhomme, 1991) and in common schemes to
 49 compute surface fluxes in mesoscale numerical weather models (Chen et al., 2010; Chen and Zhang, 2009).

50 1.2 | Roughness lengths for urban rough surfaces

51 For context, previous work linking z_{0m} and z_{0s} to geometric features of urban rough surfaces is briefly reviewed.
 52 Emphasis is placed on z_{0s} because fewer studies on scalar roughness lengths over urban surfaces have been pre-
 53 sented compared to momentum, despite their significance for turbulent fluxes in urban land-atmosphere models
 54 (Demuzere et al., 2008; Ryu et al., 2011; Wang et al., 2013; Li and Bou-Zeid, 2014). It is to be noted that roughness
 55 length models derived for vegetated canopies may not be directly extrapolated to urban surfaces. Buildings are bluff
 56 roughness elements that distinctly impact the flow when compared to permeable plants. Furthermore, the spatially
 57 heterogeneous surface temperatures and distributions of scalar sources/sinks within urban rough surfaces makes the
 58 problem of scalar roughness length determination a formidable challenge (Voogt and Grimmond, 2000; Kanda et al.,
 59 2007; Crawford et al., 2018). Nevertheless, this is a challenge that cannot be overlooked. It is of practical interest
 60 to determine z_{0m} , z_{0s} , and the corresponding bulk transfer coefficients over bluff-rough surfaces by relating them to
 61 directly-measurable surface geometrical properties (Kastner-Klein and Rotach, 2004; De Ridder, 2006; Kanda et al.,
 62 2007; Demuzere et al., 2008; Kanda et al., 2013; Zhu and Anderson, 2018). For z_{0m} , significant progress has been
 63 achieved on this front (Macdonald et al., 1998; Grimmond and Oke, 1999; Barlow and Coceal, 2009; Kanda et al.,
 64 2013; Yang et al., 2016; Kent et al., 2017; Yang et al., 2019; Zhu and Anderson, 2018) and reviewing all this literature
 65 is beyond the scope of the work here. For z_{0s} , the common approach is to relate it to z_{0m} using the quantity κB^{-1} that
 66 is assumed to vary only with the roughness Reynolds number, $Re^* = u_* z_{0m} / \nu$, where ν is the kinematic viscosity and
 67 u_* is an effective friction velocity for the urban boundary layer. However, determining this relation $\kappa B^{-1} = f(Re^*)$ so
 68 as to obtain z_{0s} remains difficult.

69 Semi-idealized field experiments using an outdoor scale-model have allowed some progress to be made (Kanda
 70 et al., 2007). In terms of the geometric effects on scalar transport, it was shown (Kanda et al., 2007) that κB^{-1} follows
 71 a universal parameterization based on a model by Brutsaert (1982) even for surfaces of different geometries. One
 72 limitation of such semi-idealized experiments is that they cannot capture other known factors that contribute to the
 73 variability of κB^{-1} such as inhomogeneous distributions of heat sources and water vapor availability as reported in
 74 field experiments at a suburban site in Tokyo, Japan (Moriwaki and Kanda, 2006a). Furthermore, vegetation fraction
 75 and anthropogenic heat sources have been shown to impact roughness parameterization (Crawford et al., 2018) but
 76 these elements were not represented in scale-model experiments. Field experiments conducted at actual urban sites
 77 face daunting challenges as well. It has been demonstrated (Voogt and Grimmond, 2000) that uncertainties related
 78 to different methodologies of surface temperature determination influence the calculated value of κB^{-1} . In addition
 79 to field experiments, wind-tunnel experiments on bluff-bodies that are heated or coated with a passive scalar have
 80 also been used for roughness length studies. For instance, cuboids coated with naphthalene (Barlow et al., 2004) or
 81 wetted with water (Ikegaya et al., 2012; Chung et al., 2015) were used to investigate the dependence of scalar transfer
 82 coefficients on roughness packing density, height variations, orientations and distributions of scalar sources.

83 Numerical approaches such as large eddy simulations (LES) are increasingly used to tackle this problems as well.
 84 Anderson (2013) simulated flow and scalar transport over different fractal surfaces finding that the usually-assumed
 85 constant value for κB^{-1} does not hold over the range of $Re_* = 10-300$. This range encompasses aerodynamically rough
 86 morphologies often encountered in the atmospheric boundary layer, except for urban morphologies. Uncertainties
 87 are invariably associated with using numerical simulations over rough walls. In particular, wall-modeled LES, which is
 88 usually applied for simulating flows in the atmospheric boundary layer, does not resolve the viscous sublayer or the

89 interfacial layer for each facet. Thus, molecular mass and heat diffusion that occurs at the interface between air and the
90 surface of the roughness elements needs to be modeled. Wall-modeled LES is currently viewed as a leading numerical
91 technique that is able to preserve the high Re of the atmosphere. Unlike momentum transfer studies where the flow
92 becomes Reynolds number independent beyond a certain high Re threshold, matching the elevated Re expected in
93 the atmosphere has been shown to be necessary when exploring scalar transfer and its connection to momentum
94 transfer (Li et al., 2016b).

95 Numerical experiments using LES over surfaces of different geometries are conducted here to address two re-
96 search objectives: the first is to examine the implications of using wall-modeled LES to infer macro-scale scalar rough-
97 ness length, and the second is to determine the scaling between κB^{-1} and Re^* and how it might depend on the
98 geometric parameters of the rough surface. To address these two objectives, the problem (Section 2) is investigated
99 by using LES results on roughness lengths for different surface geometries (Section 3). The implications on scalar
100 roughness length parameterization using surface renewal theory (Section 4) are discussed prior to the summary and
101 conclusions being drawn (Section 5).

102 2 | METHOD

103 2.1 | LES and roughness lengths

104 LES is a common technique that is widely used to simulate turbulent flow and transport over urban terrain (Kanda et al.,
105 2004; Bou-Zeid et al., 2009; Giometto et al., 2016). Direct numerical simulations (DNS), while preferred, cannot attain
106 sufficiently high $Re_b = u_* \delta_{bl} / \nu$ values representative of the atmospheric boundary layer (Slotnick et al., 2014; Li et al.,
107 2016b), where δ_{bl} is the boundary layer depth. The LES code employed here solves the equations of conservation
108 of total mass, momentum (excluding the Coriolis force), and scalar mass or thermal energy. Buildings are represented
109 using the immersed-boundary method (Appendix A). The scalar selected here is temperature. While temperature is
110 not a passive scalar *per se* and buoyancy forces could arise, we simply omit the buoyancy force term from the vertical
111 momentum equation to simulate a passive scalar in this study (i.e. the role of buoyancy remains to be explored). A
112 constant temperature (=330K) is applied to all solid surfaces, as an input to a wall-model for LES (see Eq. 4) as the
113 scalar boundary condition. However, real buildings have neither constant temperature nor flux. Use of more realistic
114 boundary conditions (e.g. coupling building energy models and radiative heat exchanges on the exterior surfaces) is
115 left for future study.

116 Two different representations of roughness lengths must be clarified. As indicated in Fig. 1, within the urban
117 boundary layer (hereafter *macro-scale*) roughness lengths z_{0m}^{mac} and z_{0s}^{mac} , as well as the zero-plane displacements, are
118 manifestations of the aggregate effects of the bluff-rough surfaces on the inertial sublayer aloft, where the logarithmic
119 mean velocity and mean air temperature profiles hold. (e.g. (Kanda et al., 2013; Yang et al., 2016)) macro-scale thermal
120 roughness lengths for flows over steep ocean waves (Sullivan et al., 2017). This needs to be distinguished from each
121 single building facet's (e.g. a roof) boundary-layer (hereafter *micro-scale*) roughness parameters. The micro-scale
122 roughness is associated with its own local velocity and temperature distribution near the surface, which follow a
123 micro-scale log-law but only in regions where the flow is facet-parallel and in equilibrium with the adjacent surface.
124 These micro-scale roughness and boundary layers in high- Re wall-modeled LES cannot be resolved (Pope, 2000), and
125 require parameterization supplied as a wall model formulation (Li et al., 2016b). Examples of such micro roughness
126 include subgrid-scale wind ripples on resolved waves (Sullivan et al., 2017) and small indentations on the surfaces of
127 built structures (Cai, 2012; Li et al., 2016b), to name a few. To add to the difficulty of the problem, it is well established
128 that the surface heat exchange parameterized using a wall model, and consequently the flow over an urban canopy, are

129 sensitive to specification of the micro-scale thermal roughness length (Cai, 2012). Therefore, if one aims to determine
 130 the macro-scale roughness length, an evaluation of the parameterization of the micro-scale exchanges is required.

131 To simplify this problem within the confines of LES, the micro-scale roughness elements are assumed to be smaller
 132 than the depth of the local viscous sublayer attached to building facets such that the LES work focuses on the macro-
 133 scale. This simplification is akin to setting all building facets as smooth walls. For an aerodynamically smooth surface
 134 in the absence of buoyancy forces, the wall-models for momentum and scalar to be used in the LES can be expressed
 135 as

$$u_*^{wm} = \frac{\kappa u}{\log \frac{z}{z_{0m}^{mic}}}, \quad (3)$$

$$\theta_*^{wm} = \frac{\kappa \Delta \theta}{\log \frac{z}{z_{0s}^{mic}}}, \quad (4)$$

137 where the superscript wm represents the wall-modeled quantities of surface stress and scalar flux $F_s = u_*^{wm} \theta_*^{wm}$; $\Delta \theta$
 138 is the difference between θ at the surface and at the first grid point away from the wall (where the flow is assumed
 139 to be already fully turbulent); and u is the wall-parallel fluid velocity at that same first grid point. The micro-scale
 140 roughness lengths z_{0m}^{mic} and z_{0s}^{mic} are set as

$$z_{0m}^{mic} = \frac{1}{9} \frac{\nu}{u_*^{wm}}, \quad z_{0s}^{mic} = \frac{1}{S_c} z_{0m}^{mic}, \quad (5)$$

141 where the constant 9 is obtained from experiments (Kader and Yaglom, 1972), $S_c = \nu/D_m$ is the molecular Schmidt
 142 number set to unity for simplicity here and D_m is the molecular diffusion coefficient for the scalar of interest. Hence, at
 143 the micro-scale, the LES assumes $z_{0m}^{mic} = z_{0s}^{mic}$. To be clear, such an LES parameterization does not resolve the viscous
 144 sublayer and does not capture the turbulence disequilibrium as the mean flow meanders around the buildings (at the
 145 micro-scale), and as such it cannot be an exact model. Log-law wall models are only accurate if the grid point nearest
 146 to the facet is within its equilibrium layer; this should hold over most of the facet areas but might be less accurate
 147 near transitions and edges. However, previous evaluation of this model for roughness elements with smooth facets
 148 indicate that it is adequate for the present purposes (Li et al., 2016b). The aim here is not to refine such wall models
 149 in the LES, which continues to be a formidable challenge (Bose and Park, 2018). Rather, the goal is to examine the
 150 implications of the aforementioned wall-model on the macro-scale scalar roughness problem with a lens on kB^{-1} .

151 2.2 | Simulation cases

152 The details about the LES code are provided in Appendix A and references therein. The grid resolution of the current
 153 setup is able to resolve the geometry of the obstacles as for most runs the number of grids resolving one obstacle
 154 is greater than six points, as shown to be sufficient with a similar code (Tseng et al., 2006). Sensitivity analysis per-
 155 formed for case VF32 (Li and Bou-Zeid, 2019) found all quantities relevant for computing the scalar and momentum
 156 displacement heights and roughness lengths change by less than 6% when the resolution is doubled. Thus, we use
 157 the current setup to allow the parameter space to be finely addressed with a reasonable computational cost.

158 Three categories of urban forms with different plan area density ($=\lambda_p$) and frontal area density ($=\lambda_f$) are considered.

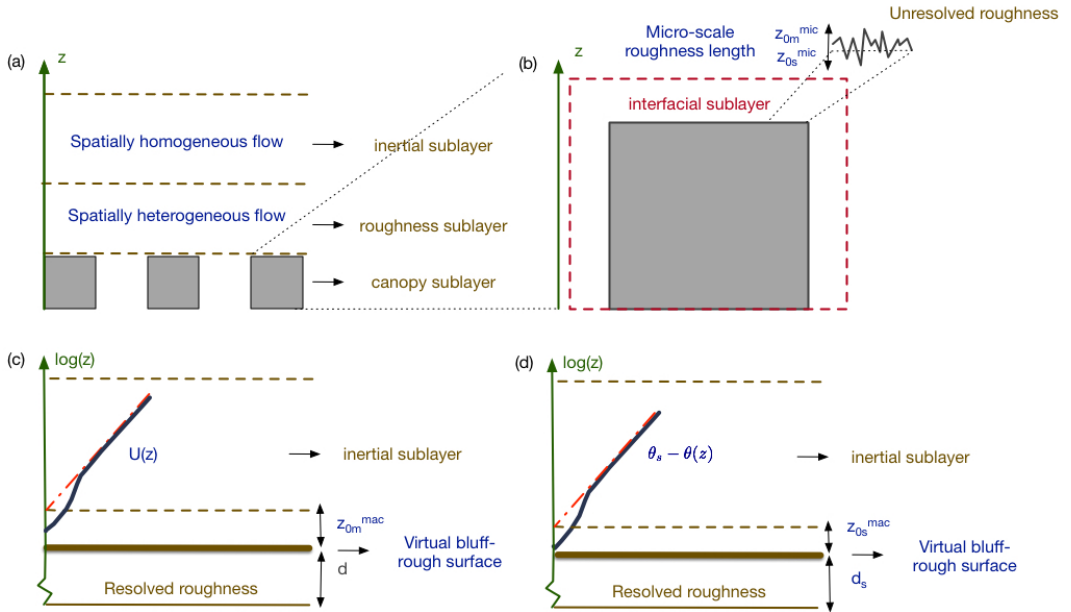


FIGURE 1 Schematic illustration of micro-scale and macro-scale roughness lengths in the LES. The LES resolves the bluff bodies present in the canopy sublayer in (a) but the facet-specific roughness elements shown in (b) are unresolved and must be represented using a wall-model of the interfacial sublayer. The micro-scale roughness lengths are imposed or parameterized in the wall model. The macro-scale roughness lengths for momentum (c) and scalar (d) have virtual origins of the logarithmic profiles of average $\langle u \rangle$ and $\langle \theta_s - \theta \rangle$. The d and d_s define the “virtual bluff-rough” surfaces that represent the aggregate effects of the resolved roughness elements. Notation is defined in the text.

159 First, (figure 2a), λ_p and λ_f are varied simultaneously but with $\lambda_p = \lambda_f$ hereafter “Variable Plan and Frontal area density”
 160 (VPF). Second (figure 2b), λ_f is maintained constant at 0.25 but λ_p is varied (Variable Plan area density, VP). Third (figure
 161 2c), λ_p is kept constant at 0.12 but λ_f is varied (Variable Frontal area density, VF). An empirical quadratic relation
 162 between λ_f and λ_p derived from Japanese building data (Kanda et al., 2013) found appreciable scatter particularly for
 163 non-Japanese cities for fixed λ_p (see their Figure 2). Hence, the category VF explores the effect of such scattered λ_f
 164 at a preset fixed λ_p . The simulation parameters for the various cases are summarized in Table 1. The focus is on the
 165 parameter space where the two characteristic densities fall between 0.1 and 0.5, reflecting the expected values for
 166 many cities and districts (Kanda et al., 2013).

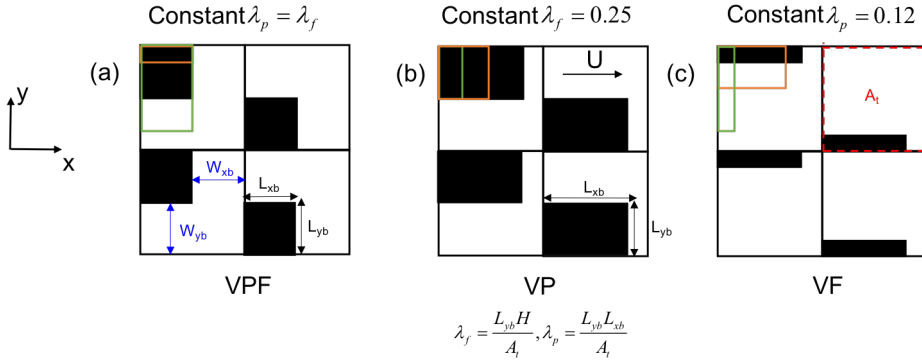


FIGURE 2 Plan area view of one “repeating unit” consisting of four buildings (black) as different geometries with a height (H) of 12.5 m. The black, orange and green lines illustrate three different possible variations of geometry within each category. (a) Variable plan and frontal area **VPF**; (b) Variable plan at a constant frontal area **VP**; (c) Variable frontal area at a constant plan area **VF**. The dimensions of the repeating units, $D_x \times D_y$, are $0.5\delta \times 0.5\delta$, $0.5\delta \times 0.5\delta$ and $0.625\delta \times 0.625\delta$ in VPF, VP and VF, respectively (see Table 1). L_{xb} and L_{yb} are the dimensions of the obstacles in the x and y directions; W_{xb} and W_{yb} are distances between adjacent obstacles in the x and y directions. Notice that for all cases $W_{xb} + L_{xb} = W_{yb} + L_{yb} = D_x = D_y$.

167 3 | ROUGHNESS LENGTHS DETERMINED FROM LES

168 Selected examples of the profiles of horizontally-averaged $\langle \bar{u} \rangle / u_*$ and $\langle (\bar{\theta}_s - \bar{\theta}) \rangle / \theta_*$ are illustrated in Fig. 3 for the
 169 VPF, VP and VF categories. Although a least-square fitting procedure to the log-law is a common approach to de-
 170 termine roughness lengths and displacement height (Kanda et al., 2004; Bou-Zeid et al., 2009; Kanda et al., 2013;
 171 Placidi and Ganapathisubramani, 2015; Yang et al., 2016). we use a ‘brute-force’ global parameter search in the $d/H -$
 172 z_{0m}/H parameter space. Additionally, $z_{0m}/H < d/H$ can be enforced when searching all parameter combinations. The
 173 optimal z_{0m}/H and d/H parameters that best fit the pre-normalized velocity $\langle \bar{u} \rangle / u_*$ (angled brackets indicate spatial
 174 averaging) are those that yield a minimum root-mean-squared error (RMSE) over the range $1.25 \leq z/H \leq 2.25$. The
 175 results and conclusions are robust to the choice of logarithmic region to perform the fitting procedure. A sensitivity
 176 analysis to the fitting range in the log-layer is shown in Appendix C; maximum deviations at the extreme fitting ranges
 177 are less than 40% relative to the adopted ranges. For all these calculations, $\kappa = 0.4$. For notational simplicity, super-
 178 scripts of macro-scale roughness length are omitted. Different procedures can lead to different computed values for
 179 d (Leonardi and Castro, 2010) and consequently of z_{0m} . For example, the “drag force moment” approach to calculate

Case	λ_p	λ_f	$\sum_i \lambda_i$	N_x^b, N_y^b, N_z^b	N_x, N_y, N_z	Re_*
VPF12	0.125	0.125	1.75	8, 4, 8	192, 96, 64	21250
VPF18	0.1875	0.1875	1.87	8, 6, 8	192, 96, 64	42930
VPF25	0.25	0.25	2	8, 8, 8	192, 96, 64	49160
VPF31	0.3125	0.3125	2.12	8, 10, 8	192, 96, 64	36290
VPF37	0.3725	0.3725	2.25	8, 12, 8	192, 96, 64	34910
VPF43	0.4375	0.4375	2.375	8, 14, 8	192, 96, 64	14096
VP12	0.125	0.25	1.75	4, 8, 8	192, 96, 64	88750
VP18	0.1875	0.25	1.875	6, 8, 8	192, 96, 64	70860
VP25	0.25	0.25	2	8, 8, 8	192, 96, 64	49160
VP31	0.3125	0.25	2.125	10, 8, 8	192, 96, 64	48220
VP43	0.4375	0.25	2.375	14, 8, 8	192, 96, 64	17850
VF08	0.12	0.08	1.76	12, 4, 8	200, 100, 64	9770
VF12	0.12	0.12	1.64	8, 6, 8	200, 100, 64	35850
VF16	0.12	0.16	1.56	6, 8, 8	200, 100, 64	78740
VF24	0.12	0.24	1.56	4, 12, 8	200, 100, 64	16504
VF32	0.12	0.32	1.64	3, 16, 8	200, 100, 64	16009

TABLE 1 Summary of simulation parameters: N_i^b is the number of nodes resolving one obstacle and N_i is the total number of nodes for the entire domain in the i direction ($i = 1$ is x or longitudinal direction, $i = 2$ is y or lateral direction and $i = 3$ is z or vertical direction). The number of nodes resolving the repeating units of dimensions $D_x \times D_y$ are 32×32 , 32×32 and 40×40 for VPF, VP and VF, respectively, where V is 'variable', P is 'plan' and F is 'frontal' area; and the last two digits represent the first two decimal values of λ_p or λ_f . $Re_* = u_* z_{0m} / \nu$, where u_* is $\sqrt{-\langle u'w' \rangle}$ defined at $z/H=1.5$ and ν is kinematic viscosity. Dimension of the computational domain normalized by the boundary layer height δ is $L_x/\delta = 3.0, L_y/\delta = 1.5, L_z/\delta = 1$ in cases VPF and VP; $L_x/\delta = 3.125, L_y/\delta = 1.5625, L_z/\delta = 1$ in cases VF.

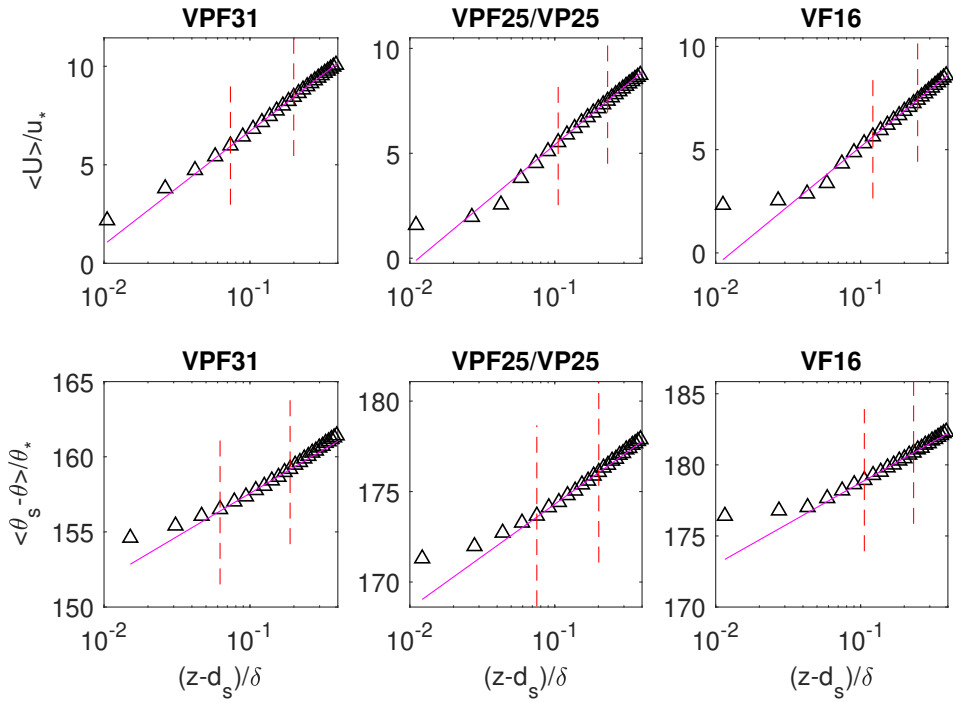


FIGURE 3 $\langle \bar{u} \rangle / u_*$ and $\langle (\bar{\theta}_s - \bar{\theta}) \rangle / \theta_*$ for three selected cases from the VPF, VP and VF, categories (*V* variable, *P* plan and *F* for frontal area). The log-law region from $z/H=1.25$ to 2.25 (red dotted vertical lines) indicate the log-laws obtained from the fitting procedure (magenta solid lines).

180 d (Jackson, 1981) and other approaches are discussed (Leonardi and Castro, 2010). As the methodology selected
 181 only have minor impact on the the momentum and scalar roughness lengths (Appendix C), it is not explored further
 182 in this study. Given the minor differences between d and d_s and minor influence on the deduced scalar roughness
 183 length, the z_{0s} is determined with $d_s = d$ (reducing the degrees of freedom in roughness length parameterizations).
 184 The densest case VP case has a d/H around unity (or slightly larger). This can be attributed to pressure drag effects
 185 extending above H , or to uncertainty in the fitting procedure. Using a von Kármán constant (κ) of 0.4, Kanda et al.
 186 (2013) found a higher d than adopting a variable κ .

187 For comparison, two models of d and z_{0m} (Macdonald et al., 1998; Kanda et al., 2013) are featured in Fig. 4. At
 188 low λ_f , there are significant differences in predicting d (both models assume d does not vary with λ_f although the LES
 189 results suggest it does), particularly for the Macdonald et al. (1998) model (Fig. 4f). The two models predict a decline
 190 in z_{0m} with increasing λ_f and decreasing λ_p , consistent with the LES-inferred values. The two-parameter (λ_p and λ_f)
 191 Macdonald et al. (1998) model surprisingly captures the responses of z_{0m} to such variable geometries considered in
 192 the LES runs (even though it failed to predict d). The surface geometries in our study fall in Mcdonald et al.'s (1998)
 193 'dense regime' (i.e. $\lambda_f > 0.03$) for all cases. The Kanda et al. (2013) model performs better overall when both d and
 194 z_{0m} are considered. For realistic highly-heterogeneous urban morphologies, more sophisticated modeling may be
 195 required. In such complex canopies, the models might need to explicitly account for the mutual interaction between
 196 roughness elements (Yang et al., 2016), or for additional statistical properties of the rough surface such as building
 197 height variance or skewness (Kanda et al., 2013; Zhu et al., 2017). Nevertheless, a morphometrically-based model
 198 appears viable to estimate z_{0m} .

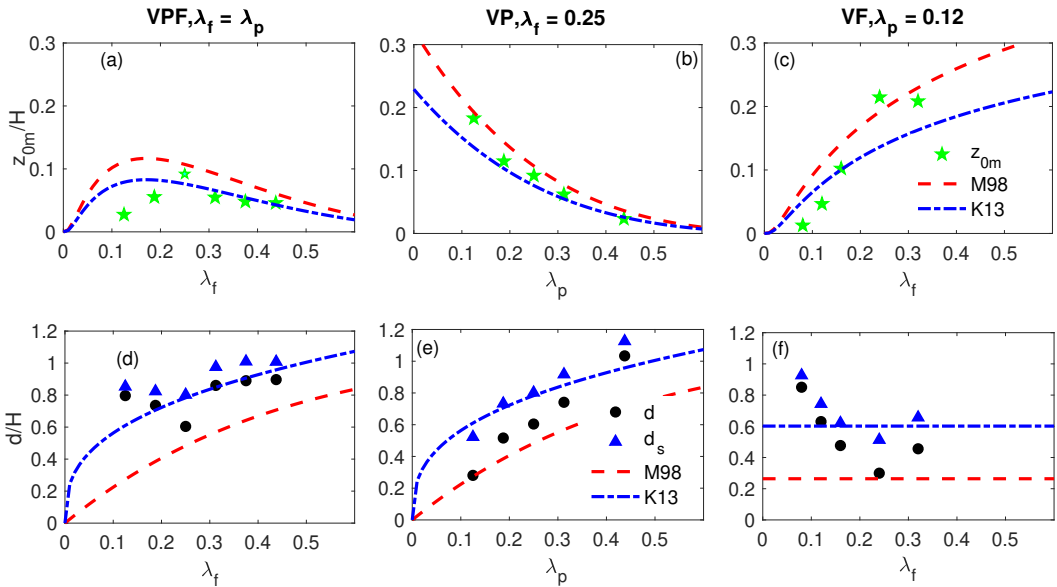


FIGURE 4 Variation of z_{0m} and d determined by direct fitting to LES output for $z/H = 1.25 - 2.25$. (a)-(c): z_{0m} and (d)-(f): d . Macdonald et al. (1998) (red-dotted line) and Kanda et al. (2013) (blue-dash-dotted line) models are also shown for categories: (a,d) VPF; (b,e) VP; (c,f) VF.

199 One interesting feature of the LES results is the opposing effects of λ_p and λ_f on z_{0m} (Fig. 4b and c) that combine

200 to explain the non-monotonic behavior in the VPF cases ($\lambda_p = \lambda_f$). Because of the opposing effects, a peak in z_{0m}
 201 is expected and occurs between $\lambda_p = \lambda_f = 0.25$ and 0.31 (see Fig. 4a). This peak in z_{0m} has been observed in many
 202 previous studies (Kanda et al., 2004; Hagishima et al., 2009; Leonardi and Castro, 2010) for arrays of cubical roughness
 203 in which λ_p and λ_f are set equal. Such non-monotonic behavior was also noted by Macdonald et al. (1998) as the
 204 obstacles become more densely packed. The peak value of z_{0m}/H is around 0.1 (Fig. 4), which is different from the
 205 cubical arrays considered by previous studies (Leonardi and Castro, 2010) reporting the peak value of z_{0m}/H to be
 206 around 0.15. This is likely caused by the obstacles in VPF not being cubes with equal dimensions in all directions,
 207 except for VPF25.

208 The variations of z_{0s} (Fig. 5a-c) between different cases overwhelmingly outweigh the effects of changes in z_{0s}
 209 when d or d_s are used in the fitting. Values of z_{0s} computed using d differ from those using d_s by less than 10%
 210 for more than half of the cases (with a highest deviation of 20%). Such differences do not change the trend of variation
 211 across cases and produce negligible change in the values of $\log(z_{0m}/z_{0s})$ (at most 0.3%). Our assumption $d = d_s$ is
 212 justifiable for the boundary conditions imposed here. As with z_{0m} , λ_p and λ_f have inverse impacts on z_{0s} , but are
 213 exactly opposite to that noted for z_{0m} . The z_{0s} increases with increasing λ_p and decreasing λ_f .

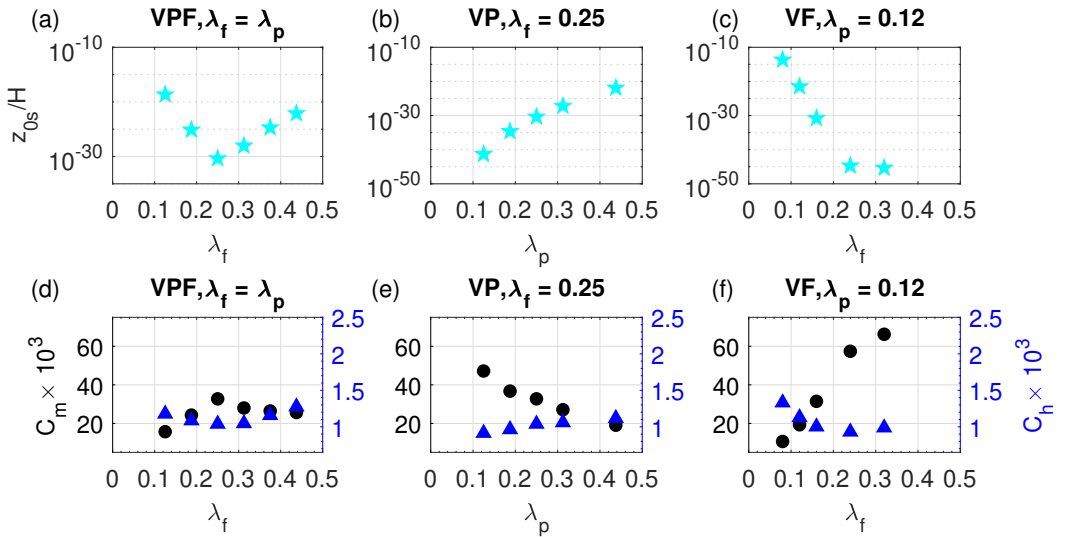


FIGURE 5 (a)-(c): The z_{0s} determined from least-square error minimization using d . (d)-(f): The bulk transfer coefficients for momentum (C_m) and scalar (C_h) computed at $z/H = 1.5$.

214 The bulk transfer coefficients for momentum and scalar are defined as

$$C_m(z) = \kappa^2 \left(\log \left(\frac{z-d}{z_{0m}} \right) \right)^{-2} \quad (6)$$

215 and

$$C_h(z) = \kappa^2 \left(\log \left(\frac{z-d}{z_{0m}} \right) \right)^{-1} \left(\log \left(\frac{z-d_s}{z_{0s}} \right) \right)^{-1}, \quad (7)$$

and are shown in Figs. 5d-f for $z/H = 1.5$. The C_m and C_h values are height dependent quantities (sometimes a factor of 2 is used in these definitions). The C_h values obtained here are within the range of scalar transfer coefficients obtained from previous wind-tunnel experiments (Barlow et al., 2004; Chung et al., 2015). A scalar transfer coefficient was derived using two-dimensional street canyon and a naphthalene sublimation technique (Barlow et al., 2004) ranges from 1×10^{-3} to 3.5×10^{-3} (see their figure 4). Likewise, a C_h that ranges between 3×10^{-3} to 3.75×10^{-3} was obtained from measurements of wetted surfaces using three-dimensional arrays of cubes (Chung et al., 2015). While uncertainty in the adopted scalar flux wall-model does affect θ_* and hence C_h , the determined C_h seems to be robust with such uncertainty. The uncertainty from the wall modeling approach to C_h is estimated to be approximately 25% (Li et al., 2016b). The differences might also be related to the lower Re in the wind tunnel experiments. As the relative change in C_h across the cases considered here exceeds 25%, the morphological dependence, at least qualitatively, still holds. The C_m and C_h combine the effects of the displacement height and roughness length on the surface exchange effectiveness, and they show independent monotonic variation with λ_p or λ_f . Their anti-correlated trends with respect to varying geometric parameters confirm that there can be significant “trade-off effects” in the effectiveness of a surface to exchange momentum or scalars with a turbulent flow.

From Eq. 7 the magnitude of z_{0s} can be understood, as C_h depends on both z_{0s} and z_{0m} even with a constant C_h , if the wall gets rougher and both pressure drag and z_{0m} increase, z_{0s} must decrease. Therefore, z_{0s} alone is insufficient to understand wall heat transfer effectiveness (C_h is better for this task). Moreover, the very small magnitudes of z_{0s} do not imply a vanishingly small heat transfer, and z_{0s} should not be interpreted as a macroscopic physical length scale or morphometric parameter. One can note, for example, that the reported values here (and elsewhere) are smaller than the mean free path of atmospheric molecules (i.e. about $70 \eta m$). This clarifies why determining z_{0s} from morphological parameters remains a daunting task for urban canopies and other surfaces as well (at least when compared to z_{0m}).

As indicated, z_{0s} is commonly obtained from z_{0s}/z_{0m} or $\kappa B^{-1} = \log(z_{0m}/z_{0s})$ as a function of Re_* . Justified on the grounds that z_{0m} is reasonably described from simplified two-parameter models (e.g. λ_f, λ_p), as confirmed here. For a variety of surfaces, including bluff-rough surfaces, a relation of the form $z_{0s}/z_{0m} \sim Re_*^n$ is used (Brutsaert, 1965, 1975b; Zilitinkevich et al., 2001; Li et al., 2017; Katul and Liu, 2017; Castellví, 2018). A variety of exponents ($n=0, 1/4$ or $1/2$) and intercepts have been reported across differing surfaces. Their universal character is questioned in several studies. The next section discusses such parameterization using a phenomenological model based on surface renewal theory, which has rarely been applied to urban canopies. Its development here constitutes one of the main theoretical novelties of this paper.

4 | SCALAR ROUGHNESS LENGTH FROM SURFACE RENEWAL THEORY

Since Danckwerts (1951) first introduced a statistical model that accounts for duration over which eddies are in contact with an interface (i.e. interval between renewals), extending the surface renewal theory (SRT) to model turbulent transport of scalars in the atmospheric boundary layer has been the subject of inquiry for the past 40 years (Brutsaert, 1975b; Clayson et al., 1996; Katul et al., 1996; Snyder et al., 1996; Denby and Snellen, 2002; Katul et al., 2006; Castellví et al., 2008; Li et al., 2017). Most applications of the SRT are limited to the “natural” rough and smooth surfaces such as the ocean surface (Clayson et al., 1996), glacier surfaces (Denby and Snellen, 2002), grasslands (Li et al., 2017) and forests (Katul et al., 1996). Whether the surface renewal concept is applicable to *very rough* surfaces that consist of large bluff-body objects such as buildings is now considered within the context of interfacial scalar transfer.

256 4.1 | Basics of Surface Renewal Theory

257 The basic assumptions common to all SRT schemes are briefly reviewed. A parcel of air sweeps to the surface and
 258 is in contact with the surface for a random duration s . During the interval s , the parcel exchanges mass or heat with
 259 the surface via molecular diffusion only. After s , the parcel is ejected and is replaced by a new parcel. In the sim-
 260 plest SRT, this repeated sweep-ejection-replacement process leads to what is labeled as 'continuous surface renewal'.
 261 The distributional properties of s , $\phi(s)$ must be externally supplied and are assumed to follow an exponential form
 262 (Danckwerts, 1951). Other forms (e.g. log-normal, power-law, Gamma, Inverse-Gaussian) have also been proposed
 263 with various justifications (Katul and Liu, 2017). The choice $\phi(s) = R \exp(-Rs)$ is the simplest and most convenient
 264 - it defines the probability density function for the rate of occurrence of a surface renewal event and satisfies the
 265 normalizing property $\int_0^\infty \phi(s) ds = 1$. This one-parameter probability density function requires only the specification
 266 of $1/R$. Physically, $1/R = \int_0^\infty s\phi(s) ds$ is the mean time that an eddy remains in contact with the surface before it is
 267 ejected away. In general, $\phi(s)$ must only depend on the flow properties, not the scalar being analyzed. The exact
 268 functional form of $\phi(s)$ appears not to be as crucial as the specification of $1/R$ - at least for mean flux calculations
 269 as discussed elsewhere (Katul and Liu, 2017). In all SRT versions, the scalar transfer at the surface over a contact
 270 duration s is, as earlier noted, assumed to be via molecular transfer characterized by D_m and a local gradient at the
 271 surface during event s . To a leading order, this near-surface concentration gradient during s can be approximated
 272 by $(\Delta\theta')/\sqrt{D_m s}$, where $\Delta\theta'$ is assumed to be primarily dominated by mean scalar changes within the local interfacial
 273 layer with a characteristic thickness $\sqrt{D_m s}$ (the layer bounded by red dotted line in Fig. 1b; i.e. at the micro-scale and
 274 accommodated only in the wall model of the LES).

275 With the choice of the distribution function $\phi(s) = R \exp(-Rs)$, the mean thickness of the local interfacial layer
 276 is L_i given by

$$L_i \propto \int_0^\infty \phi(s) (D_m s)^{1/2} ds = \frac{1}{2} \sqrt{\frac{\pi D_m}{R}}. \quad (8)$$

277 Mean temperature changes from L_i to any height above L_i are assumed to be minor when compared to $\Delta\theta'$ within
 278 L_i . This is required in SRT because differences in temperatures of air parcels originating from outside this interfacial
 279 layer are not explicitly considered, and $\Delta\theta'$ is thus strictly controlled by the surface flux. With this background, the
 280 heat flux summed over all random contact times must be given as

$$F_c = - \int_0^\infty \phi(s) D_m \left(\frac{\partial \theta}{\partial z} \right)_{z=0} ds \propto -D_m \int_0^\infty R \exp(-Rs) \frac{\Delta\theta'}{(D_m s)^{1/2}} ds. \quad (9)$$

281 This expression can be arranged to yield

$$Sh = \frac{F_c}{u_* \Delta\theta'} = \frac{1}{u_*} A \pi D_m^{1/2} R^{1/2}, \quad (10)$$

282 where Sh is the Sherwood number (a type of a mass transfer Stanton number) and A is a proportionality constant.
 283 When the total scalar or heat fluxes and u_* are constant with z and the primary $\Delta\theta'$ is across the interface, the
 284 Sh can be interpreted as both an interfacial and a bulk (i.e. extending to the inertial layer, not just the interfacial
 285 layer) characteristic. These assumptions are common to virtually all SRT. The main difference between various SRT
 286 approaches is broadly in how $1/R$ is specified. It is thus instructive to analyse these approaches using two 'end-
 287 member' cases: the micro-eddy and macro-eddy models (Fig. 6) characterizing $1/R$.

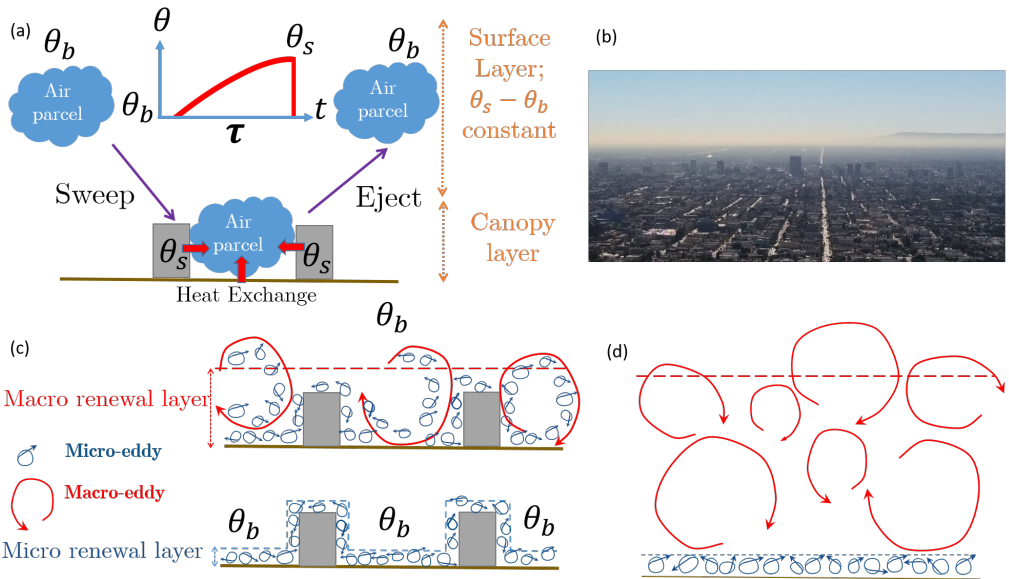


FIGURE 6 A schematic illustrating the (a) continuous surface renewal theory (SRT) process and (b) a typical urban bluff-rough surface. (c) concepts of the micro-scale and macro-scale eddies viewed in the context of SRT, and (c) with bluff bodies and (d) without bluff bodies. For the micro-eddy model, it is assumed that the limiting step in the scalar exchange process is availability of Kolmogorov eddies that can populate the entire surface area. For the macro-eddy model, the ability to produce or bring Kolmogorov eddies to the exchanging surface by macro-eddies is considered to be the limiting step.

288 4.2 | The micro-eddy model

289 In the micro-eddy model, it is assumed that large eddies can be efficient in bringing air parcels (and small eddies) near
 290 the solid interface but do not interact with the interface. Heat or mass exchange at the solid interface must only
 291 occur after air parcels penetrate and momentarily break-up the viscous sublayer and make direct contact with the
 292 solid surface. Hence, we take the view that only the smallest of eddies (active in the viscous and buffer layers) are
 293 sufficiently efficient at penetrating the viscous sublayer to interact with the surface. According to the micro-eddy
 294 model, this efficiency is not based on the energy content of an eddy. If an eddy is sufficiently energetic to penetrate
 295 into or displace the viscous sublayer, any excess kinetic energy carried by the eddy is not used in the renewal and
 296 its interaction with the surface will not depend on this excess. Hence, the micro-eddy model assumes that it is the
 297 collision frequency between eddies and the viscous sublayer that dictates the renewal frequency, not the energy
 298 content of eddies. Very small eddies in the vicinity of the interface are expected to experience collision events with
 299 the viscous sublayer at a high frequency when compared to large eddies. Because of the high frequency of collisions,
 300 the very small eddies encounter the viscous sublayer far more frequently (at least compared to their much larger eddies
 301 counterparts) and contribute to scalar mass exchange. In the energy cascade, these small eddies are commensurate
 302 in size with the so-called Kolmogorov viscous length scale (Brutsaert, 1965). Under such a condition, $1/R$ is assumed
 303 to scale with the Kolmogorov time scale $= (\nu/\epsilon)^{1/2}$, where ϵ is the mean turbulent kinetic energy dissipation near the
 304 interface. With $R = (\nu/\epsilon)^{-1/2}$ (flow and fluid properties) and $D_m = Sc^{-1}\nu$,

$$Sh = \frac{F_c}{u_* \Delta \theta'} = \frac{1}{u_*} A (\pi Sc^{-1})^{1/2} (\nu \epsilon)^{1/4}, \quad (11)$$

305 where $(\nu \epsilon)^{1/4}$ is the Kolmogorov velocity with an associated kinetic energy $= (\nu \epsilon)^{1/2}$.

306 This micro-eddy model thus postulates that the canyon sublayer air in between the buildings has comparable
 307 scalar concentration to the roughness and inertial layer air, and that the micro eddies then sweep this canopy layer
 308 air in contact with various facets where it is further enriched in scalar concentrations. To place this result in the
 309 context of prior theories (Brutsaert, 1965), the following representation of the cuboid surface can also be made. The
 310 cuboids-air interface is first replaced by an equivalent rough surface (i.e. experiencing the same scalar flux and u_*)
 311 characterized by z_{0m} and positioned at $z = d$ (Fig. 1c thick brown line). For this rough surface, the turbulent kinetic
 312 energy dissipation rate inside the equivalent roughness elements (characterized by z_{0m}) is assumed to be given by the
 313 balancing mechanical production term (i.e. assuming local equilibrium)

$$\epsilon = u_*^2 \frac{du}{dz} \propto u_*^2 \frac{u_*}{\kappa z_{0m}}. \quad (12)$$

314 For these assumptions, it directly follows that

$$Sh = A' Sc^{-1/2} (Re_*)^{-1/4}, \quad (13)$$

315 where A' is another similarity constant. Hence, the micro-eddy model (Brutsaert, 1965) predicts a $Sh \propto Re_*^{-1/4}$. For
 316 most trace gases (or temperature), Sc (or the Prandtl number Pr) is near unity in air and plays a lesser role (it was
 317 assumed unity in the LES here). Another important feature of the micro-eddy model is that the resulting $L_j \propto Sc^{-1/2} \eta$
 318 (i.e. the Batchelor length), where $\eta = (\nu^3/\epsilon)$ is, as before, equal to the Kolmogorov length scale. This scale is not
 319 resolved in the LES but is represented by the wall model.

4.3 | The macro-eddy model

In this representation, the limiting step to heat or scalar exchange is assumed to be the efficiency of large coherent eddies to deliver parcels of air to the surface that then enable Kolmogorov eddies to exchange heat with the interface. The canopy sublayer air has a significantly higher concentration than the roughness sublayer air aloft, and surface renewal requires a large eddy to penetrate into, and ventilate, the canopy layer to sustain surface fluxes. Previous studies over large bluff-body obstacles (Leonardi et al., 2015) demonstrated that organized eddy motions indeed dominate in the roughness and canopy sublayers for turbulent scalar transport. For ‘obstructed shear flows’ (Ghisalberti, 2009) such as flows over urban canopies, the canopy flow can be characterized by the penetration depth (L_s) of the vortices into the canopy sublayer. These can be linked to the shear length scale defined as $L_s = \frac{\bar{u}}{d\bar{u}/dz}$ for $z = H$ at the mean canopy height (Raupach et al., 1996). For most canopies, except the sparse ones, $L_s \leq H$ and in general L_s is of the order of H (Raupach et al., 1996; Katul et al., 1998; Poggi et al., 2004; Li and Bou-Zeid, 2019). The characteristic mean contact time scale can be related to the mean vorticity time scale, $(d\bar{u}/dz)^{-1}$ at $z = H$, which is L_s/U_H , where $U_H = \bar{u}(z = H)$. In addition, if the log-profile is extrapolated to $z = H$, $d\bar{u}/dz \approx u_*/(\kappa z_{0m})$. Indeed, the LES results depicted in Fig. 7a confirm that $(d\bar{u}/dz)^{-1} = L_s/U_H$ is correlated with u_*/z_{0m} (correlation coefficient is 0.73 with a p-value = 0.001). For this macro-eddy model, the characteristic mean contact time of renewal is proportional to the mean vorticity time scale (instead of the Kolmogorov time scale). Conceptually, this assumption implies that each single large coherent eddy leads to a single renewal event of the canopy sublayer air, and the number of renewal events must be identical to the frequency of occurrence of coherent events. Meanwhile, numerous other turbulent events, including Kolmogorov-sized eddies, renew the viscous sublayer multiple times but they are not the bottleneck in the renewal process (as their generation and delivery is dependent on the macro-eddy). This physical picture implies that large canopy-layer air ventilation events control the renewal rate, and that the entire building facet area then exchanges heat or scalars with each coherent eddy. Stated differently, the renewal eddy is ‘space-filling’ over a large contact area in this macro-eddy model. One can then contrast this to the micro-eddy model where numerous Kolmogorov eddies are assumed to be present at all points in the flow domain including all points around building facets.

Mindful of these physical assumptions, this macro-eddy model leads to

$$\frac{1}{R} \sim \frac{L_s}{U_H} \sim \kappa \frac{z_{0m}}{u_*}. \quad (14)$$

Now that the rate of surface renewal from macro eddies is estimated, it directly follows from Eq. 10 that

$$Sh = A'' S c^{-1/2} R e_*^{-1/2}. \quad (15)$$

Therefore, the differing assumptions between the micro- and macro-eddy models result in distinct scaling laws between Sh and Re_* .

4.4 | The chain-saw model

This model was originally formulated to explore air-water gas exchange in streams (Moog and Jirka, 1999). The basic assumptions can be contrasted to the urban roughness exchange mechanisms discussed here. In its original form, surface renewal is analogous to a chain-saw cutting a tree. The small teeth of the chain-saw perform the actual cutting (much like the Kolmogorov eddies cutting through the viscous sublayer in the micro-eddy approach) but the

354 chain speed and the larger saw blade (much like the large and coherent eddies) carry the small-teeth to the cutting zone
 355 (the viscous sublayer attached to solid boundaries). Both the speed of the chain and the access of the small blades to
 356 the cutting zone control the actual cutting. Both scales 'cooperate' and can now be incorporated for urban roughness
 357 by adopting the active zones approach of the chain saw model. In this case, each eddy penetration encounters an
 358 incomplete interfacial area not covering the entire surface area. The chain-saw model then assumes that within each
 359 patch area covered by the big eddy, Kolmogorov (or Batchelor) sized eddies carry out the scalar exchange as in the
 360 micro-eddy model. The micro-eddy model still represent the correct physics but must be amended to include the
 361 'active zone' fractional area A_a^+ reflecting the penetration and renewal from large eddies. It is straightforward to show
 362 that this representation leads to

$$Sh = A' Sc^{-1/2} (A_a^+) (Re_*)^{-1/4}, \quad (16)$$

363 where A_a^+ is now expected to scale with Re_* and the arrangement of the roughness elements. If $A_a^+ \sim Re_*^0$, then the
 364 micro-eddy model is restored, whereas with $A_a^+ \sim Re_*^{-1/4}$, the macro-eddy model is recovered.

365 In the chain-saw model, at a fixed Sh and for an imposed u_* dictating the energy available for eddy penetration
 366 into the canopy elements (set by u_*^2), increasing z_{0m} increases Re_* but reduces the eddy penetration and hence A_a^+ . The
 367 chain-saw model is featured here not because of its prognostic skills - but its diagnostic skills. It suggests that a number
 368 of possible exponents are possible depending on how efficient the eddy penetration into the cuboids is. Another
 369 amendment to the chain-saw model may include the spatial intermittency of ϵ at the walls of the cuboids for each
 370 eddy penetration, adding another relation between Re_* and ϵ . The scaling of A_a^+ with Re_* is rarely studied in urban
 371 canopies and must be externally supplied for now. Nonetheless, the analysis here provides plausible explanations as
 372 to why differing scaling exponents for $Sc - Re_*$ may have been reported in the literature.

373 4.5 | Linking Surface Renewal to κB^{-1}

374 As noted, the Sh derived from SRT can be interpreted as both an interfacial and bulk characteristic extending to the
 375 inertial layer. If so, Sh can then be determined from equation 2 in the neutral limit as

$$Sh^{-1} = \frac{1}{\kappa} \log \left(\frac{z - d_s}{z_{0s}} \right). \quad (17)$$

376 Similarly, the interfacial bulk drag coefficient for the virtual bluff-rough surface C_m , Eq. 6, can be related to z_{0m} as

$$C_m^{-1/2} = \frac{1}{\kappa} \log \left(\frac{z - d}{z_{0m}} \right). \quad (18)$$

377 Then, assuming $d = d_s$, z_{0m} and z_{0s} can be related using Sh and C_m using

$$z_{0s} = z_{0m} \exp \left[-\kappa \left(Sh^{-1} - C_m^{-1/2} \right) \right], \quad (19)$$

378 in which $Sh^{-1} - C_m^{-1/2}$ is usually referred to as B^{-1} , i.e. $z_{0s} = z_{0m} \exp [-\kappa B^{-1}]$. For the macro-eddy model, the B^{-1}
 379 can be expressed as:

$$B^{-1} = Sh^{-1} - C_m^{-1/2} = A_1 Re_*^{1/2} - C_m^{-1/2} = A_1 Re_*^{1/2} + A_2, \quad (20)$$

where A_1 is $1/A'$, and $A_2 = -C_m^{-1/2}$. In the fully rough limit at high Re , C_m only depends on the geometry of the surface and should become Reynolds-number independent (equivalent to stating that d and z_{0m} are independent of wind speed and fluid viscosity). It is also worth noting that the A_2 parameter obtained as the intercept from field data using statistical regression (Kanda et al., 2007) has a clear physical meaning that pertains to the bulk drag coefficient as $A_2 = -C_m^{-1/2}$, and it is constant only under the assumption of C_m being a much weaker function of Re_* than Sh .

Fig. 7a shows the calculated B^{-1} from LES for all the three-dimensional rough surfaces in Table 1; models from Brutsaert (1965, 1975a) and Kanda et al. (2007) are also shown. The model by Brutsaert (1965, 1975a) is based on the micro-eddy model and results in $B^{-1} = C_1 Re_*^{1/4} + C_2$ instead of $Re_*^{1/2}$ for the macro-eddy model. The model by Kanda et al. (2007) assumes the same one-fourth power relation between B^{-1} and Re_* . These models with an exponent $\approx 1/4$ do not seem to be the most appropriate for the large bluff roughness elements of this study despite the fact that they were reported to match observations better (than ones with exponents $\approx 1/2$) over natural surfaces such as waves (Li et al., 2018). We could improve these models by refitting their constants to the LES data, but given the mismatch in the slope this was deemed unnecessary. The macro-eddy model captures the LES derived $B^{-1} - Re_*$ scaling better. Additional relevant models in the literature are shown in Table 2. Zilitinkevich et al. (2001) obtained $Re_*^{1/2}$ scaling, but the result was derived based on dimensional analysis without invoking surface renewal theory (yet it matches the macro-eddy model in scaling).

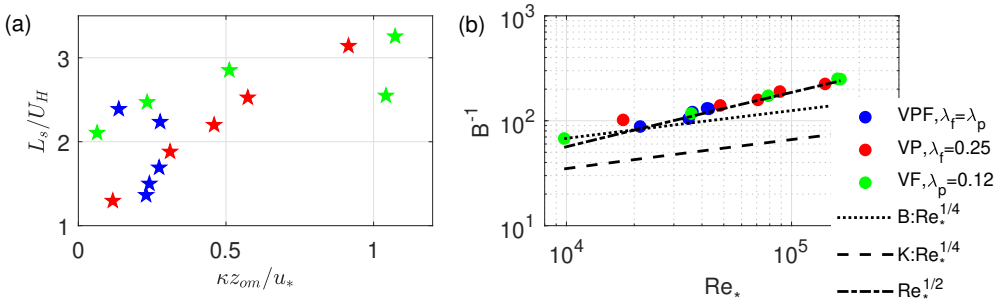


FIGURE 7 (a) The relation between L_s/U_H and $\kappa z_{0m}/u_*$ showing reasonably-linear trends. The macro-eddy model assumes that the mean contact time $1/R$ can be estimated as $\kappa z_{0m}/u_*$. (b) B^{-1} as a function of $Re_* = u_* z_{0m}/\nu$ from LES and various models. The SRT predictions from the micro-eddy and macro-eddy models are also shown. B: $Re_*^{1/4}$ Brutsaert (1975b) model: $7.3Sc^{1/2}Re_*^{1/4} - 5$. K: $Re_*^{1/4}$ Kanda et al. (2007) model: $6.4Re_*^{1/4} - 5$. $Re_*^{1/2}$ least-square regression of the macro-eddy power law model: $B^{-1} = Sh^{-1} - C_m^{-1/2} = 0.60Re_*^{1/2} - 3.5$.

A least-square regression with $Re_*^{1/2}$ yields the constants $A_1 = 0.68$ and $A_2 = 3.5$ (Table 2, Method 1). Least-square fitting of $Sh^{-1} \propto Re_*^{1/2}$ and $Sh^{-1} \propto Re_*^{1/4}$ found that the $1/2$ scaling yielded a coefficient of determination of 0.96 (cf. 0.80 for the $1/4$ scaling). This finding confirms that the SRT with the macro-eddy representation is consistent with the wall-modeled LES computations of macro-scale scalar roughness length. It should also be noted that B^{-1} versus Re_* can have a large range of variability (cf. Figure 6 in Kanda et al. (2007), Figure 2 in Crawford et al. (2018)), which can be attributed to variability in the multiplicative factor A_1 or from other physical processes not captured here that could also alter the power exponent relating B^{-1} and Re_* .

The functional dependence between Sh^{-1} and Re_* (Fig. 8) can now be exploited to propose a new approach to parameterize z_{0s} for urban terrain. Morphometric models, (e.g. Kanda et al. (2013) can be used to obtain z_{0m} and d , and therefore compute $C_m^{-1/2}$, according to Eq. 18 for a given z). Using Eq. 20 with $A_1 = 0.70$ deduced from LES

406 here, (or fit other observational or LES data for other distinct geometries), z_{0s} results are obtained (Table 2, Method 2).
 407 Direct evaluation of z_{0s} obtained from LES in Fig.8b (we compare the logarithms since they are the forms that appear
 408 in conventional models) have good agreement.

Reference	B^{-1}
Owen and Thomson (1963)	$2.40Re_*^{0.45}$
Brutsaert (1975a)	$7.3Sc^{1/2}Re_*^{1/4} - 5$
Cahill et al. (1997)	$4.31Re_*^{1/4} - 5$
Zilitinkevich et al. (2001)	$0.5Re_*^{1/2} - 3.2$
Method 1: Eq. 20 with constant A_2	$0.60Re_*^{1/2} - 3.5$
Method 2: Eq. 20 with variable $A_2 = -C_m^{-1/2}$ from morphometric model	$0.70Re_*^{1/2} - C_m^{-1/2}$

TABLE 2 Relation between B^{-1} and roughness Reynolds number Re_* from different studies.

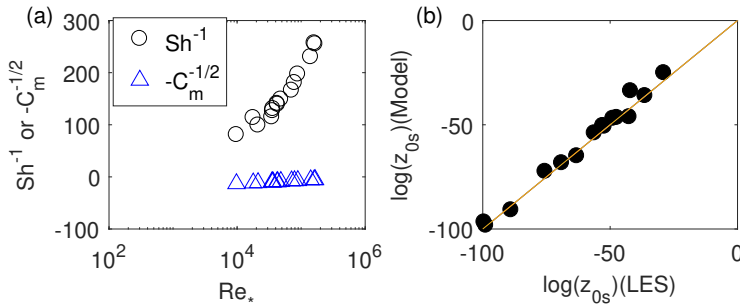


FIGURE 8 Variations of Sh^{-1} and $C_m^{-1/2}$ with Re_* (a) and scalar roughness length z_{0s} modelled (Method 2, Table 2) versus results directly from LES.

409 5 | CONCLUSIONS

410 Large-eddy simulations for urban surfaces consisting of arrays of large cuboids are conducted to address how urban
 411 roughness elements impact the variations of scalar roughness length when compared to its momentum counterpart.
 412 The simulations had frontal area density λ_f and plan area density λ_p varied independently. The variations in z_{0m} are
 413 linked to the combination of increasing with λ_f and decreasing with λ_p . Models based on morphometric parameters
 414 have acceptable predictive power to capture these trends for z_{0m} . To link such models for z_{0m} to z_{0s} , the $\kappa B^{-1} =$
 415 $\log(z_{0m}/z_{0s}) = A_1 Re_*^n + A_2$ framework was used. An approach based on the surface renewal theory is proposed
 416 to determine n . The exponent derived here closely follows its theoretical prediction when the mean contact time is
 417 derived from macro-eddy properties ($n = 1/2$) instead of micro-eddy properties ($n = 1/4$). An alternative model that is
 418 based on the chain-saw analogy was also explored. This model features an effective contact area depending on eddy
 419 penetration, and can recover either the micro- or macro-eddy models scaling, depending on how this area scales with

420 Re_* .

421 The results here have three major implications:

422 (i) There are “trade-off effects” in the effectiveness of a very-rough surface in exchanging momentum and scalars
 423 with a turbulent flow as can be deduced from the opposing trends of C_m and C_h with changes in geometry. Similar
 424 findings have been reported over steep waves (Sullivan et al., 2017). These findings illustrate the contrasting effects
 425 of roughness elements, as discussed by Brutsaert (1975b) and others: “... (roughness elements) on the one hand, they
 426 act as windbreaks, reducing surface exposure and thus transfer, while on the other hand, they increase drag and thus
 427 shear with a concomitant increase in eddy diffusivity”. Roughness elements are usually applied to a smooth wall to
 428 increase turbulence mixing, which enhances both drag and heat transfer. For urban surfaces, the results here imply
 429 that as the density of roughness elements increases, a point will be reached beyond which convective heat transfer
 430 will become less efficient. Similarly, skin hairs promote heat transfer at low densities but acts as insulators at higher
 431 densities (Fowler and Bejan, 1995).

432 (ii) In contrast to land surface models that postulate a relation $z_{0s} \propto z_{0m}$ (usually with a pre-factor of 1/10), the
 433 LES predicts that an increase in z_{0m} results in a decrease z_{0s} . In addition, the macro-eddy SRT model proposed in this
 434 paper, as well as all other models evaluated here (including those closely following the micro-eddy SRT) also predict an
 435 inverse relation of the two roughness lengths (for typical values of the friction velocity, air viscosity and momentum
 436 roughness length in urban terrain; Fig. 9a with a friction velocity $u_* = 1 \text{ m s}^{-1}$). Different values u_* values dictate
 437 changes in z_{0s} as z_{0m} varies, which gives rise to the scatter in LES results shown in Fig. 9b. Data from other studies
 438 are also shown in Fig.9b. Despite the large range of uncertainty, that z_{0s} decreases with increasing z_{0m} is consistent
 439 with these data.

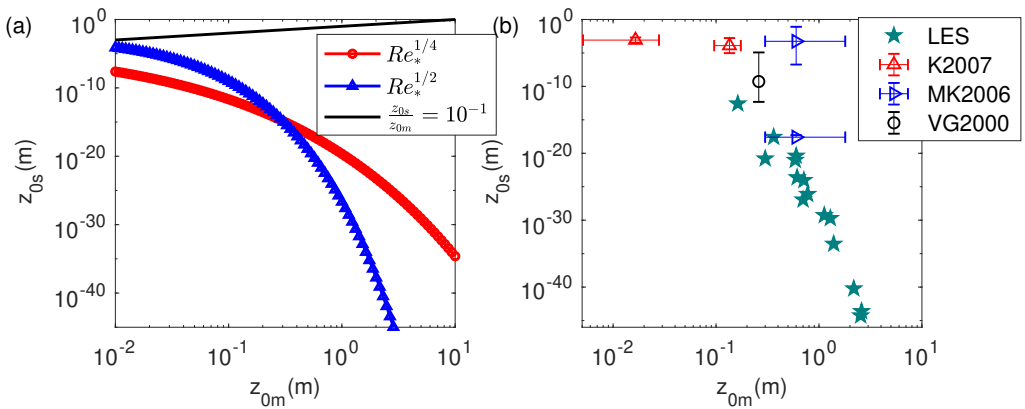


FIGURE 9 (a): Variation of z_{0s} with z_{0m} for a typical friction velocity $u_* = 1 \text{ m/s}$, $\nu = 1.46 \times 10^{-5} \text{ m}^2/\text{s}$. z_{0s} modeled with Brutsaert (1975a) (red circle); z_{0s} modeled with Method 1 in this study (blue triangle); $z_{0s}/z_{0m} = 10^{-3}$ (black line). (b): LES and previous field measurements. LES (teal stars); K2007 (red triangle): outdoor urban scale models in Kanda et al. (2007), the whiskers indicate standard deviations of momentum and heat roughness lengths reported in Table 3 of Kanda et al. (2007); MK2006 (blue triangle): measurements from a suburban site in Tokyo, Japan by Moriawaki and Kanda (2006b) showing momentum, heat (upper triangle) and water vapor (lower triangle) roughness lengths reported in Table 1 of Moriawaki and Kanda (2006b), where the whiskers indicate their respective standard deviations; VG2000 (black circle): measurements from a light industrial site in Vancouver, British Columbia, Canada from (Voogt and Grimmond, 2000). Data are extracted from their Fig.8a, where the whiskers indicate the range of heat roughness lengths.

440 (iii) As obstacle-resolving LES is becoming a promising tool to explore urban atmospheric boundary layers. How-
 441 ever, how to interpret the bulk transfer properties directly computed from LES, especially for scalars, remains a subject
 442 of inquiry. The values that emerge from the analysis can depend on the wall-model used to link the obstacle surface
 443 to the flow. The wall-model formulation used here is self-consistent with expected theoretical behavior of an aerody-
 444 namically smooth wall, as well as the micro-eddies in the surface renewal theory (Appendix B).

445 (iv) The feasibility of estimating z_{0s} for urban surfaces using a two-step approach is demonstrated. This should
 446 be verified, using field observations and/or LES or DNS, for other more realistic geometries. This method utilizes the
 447 Re_* dependence of scalar transfer and the adequate skill of the existing morphometric momentum roughness length
 448 models. Here only Macdonald et al. (1998) is used to illustrate this two-step approach to compute C_m . Future studies
 449 could use newer models (e.g. (Kanda et al., 2013; Yang et al., 2016; Zhu and Anderson, 2018), etc.) for d and z_{0m} to
 450 further refine C_m .

451 Although the number of cases with idealized cuboids is limited, the generalized framework of both micro- and
 452 macro-scale roughness lengths can be extended and tested for other configurations (e.g. a larger morphometric pa-
 453 rameter space and realistic urban geometries). In addition, the impact of different thermal boundary conditions and
 454 atmospheric stability regimes have been purposely omitted, but these effects are expected to have a significant influ-
 455 ence on d , z_{0m} , and z_{0s} . Last, the 'chain-saw' model for surface renewal opened up the inquiry into how to connect
 456 the penetration of eddies into the roughness elements with Re_* and whether the turbulent kinetic energy dissipation
 457 rate is spatially intermittent with patchy contact wall areas that scale with Re_* . Recent advances in thermal infrared
 458 imaging may offer some clues on how to proceed; this is also a topic that can be explored using DNS in future studies.

459 Appendix A: Numerical setup

460 The LES model used here implements the immersed boundary method (IBM) to resolve the bluff-body obstacles
 461 explicitly. The non-dimensional filtered incompressible continuity (A 1), Navier-Stokes (A 2) and scalar conservation
 462 (A 3) equations are solved assuming hydrostatic equilibrium of the mean flow:

$$\frac{\partial u_i}{\partial x_i} = 0, \quad (\text{A } 1)$$

$$\frac{\partial u_i}{\partial t} + u_j \left(\frac{\partial u_i}{\partial x_j} - \frac{\partial u_j}{\partial x_i} \right) = -\frac{\partial p}{\partial x_i} - \frac{\partial \tau_{ij}}{\partial x_j} + F_i + B_i, \quad (\text{A } 2)$$

$$\frac{\partial \theta}{\partial t} + u_i \frac{\partial \theta}{\partial x_i} = -\frac{\partial q_i^s}{\partial x_i}, \quad (\text{A } 3)$$

465 where x , y and z denote the streamwise, cross-stream and wall-normal directions respectively, and u , v and w are
 466 the velocity components in these respective directions; t denotes time; u_i is the resolved velocity vector; p is the
 467 modified pressure; τ_{ij} is the deviatoric part of the subgrid stress tensor; F_i is the body force driving the flow (here
 468 simply a homogeneous steady horizontal pressure gradient imposed along the x direction); and B_i is the immersed
 469 boundary force representing the action of the obstacles on the fluid. In equation (A 3), θ denotes the concentration
 470 of a passive scalar quantity and q_i^s is the i^{th} component of the subgrid scale scalar flux. All the variables used are the
 471 filtered components, although the usual tilde on top is omitted for notational simplicity. Equations A 1 to A 3 are
 472 pre-normalized by the friction velocity that accounts for the total (viscous and form) surface drag (u_*), the boundary-layer
 473 depth (δ), air density (ρ) and a reference scalar quantity (θ_0).

474 The passive scalar θ considered here is temperature, but the buoyancy force is omitted to mimic a passive scalar
 475 (the gravitational acceleration is set to zero); the results would be applicable to all other nearly-passive scalars such
 476 as water vapor. However, future extension to include buoyant forces under strong heating is required to proceed to-
 477 wards realistic conditions. An isothermal boundary condition of 330K is imposed on all surfaces. Horizontal periodic
 478 boundary conditions are applied to all quantities. The top boundary conditions are zero stress and scalar flux and
 479 no-penetration (zero normal velocity). Further details regarding the numerical procedures are described elsewhere
 480 (Chester et al., 2007; Li et al., 2016a) and the subgrid scale model is discussed in Bou-Zeid et al. (2005). The code has
 481 been verified (Li et al., 2016a,b) for its performance in simulating both momentum- and scalar- transport. All simu-
 482 lations are run for 50 eddy turn-over times defined as δ/u_* and the last 25 are averaged for the statistics analyzed here.
 483

484 **Appendix B: The relation between wall-modeled F_s and z_{0s}^{mic}**

485 Implications of micro-scale roughness values in the LES wall-model in terms of F_s (the scalar fluxes computed from
 486 the wall model) are considered. The surface renewal theory (Brutsaert, 1982) for surfaces that are aerodynamically
 487 smooth or having intermediate roughness elements indicate a sub-linear dependence on friction velocity ($\propto u_*^{3/4}$) of
 488 surface fluxes of passive admixtures. Such a sub-linear dependence discussed elsewhere (Katul and Liu, 2017) has
 489 been shown not to depend on the assumptions intrinsic to surface renewal theory. For example, the mean flux of a
 490 passive scalar admixture (e.g. water vapor) (Katul and Liu, 2017) is :

$$491 F_s \propto D_m^{1/2} u_*^{3/4} (\kappa \nu z_{0m}^{mic})^{-1/4} (\theta_s - \theta_h), \quad (B 1)$$

492 where D_m is molecular diffusivity of water vapor; θ_s and θ_h are mean scalar concentration (or temperature) at the
 493 surface and interfacial sublayer, respectively. Physically, the micro-scale roughness length is a bulk representation of
 494 the thickness of the interfacial sublayer and of (i) either the molecular processes therein for smooth walls, or (ii) of the
 495 roughness geometries of the surface for intermediate rough walls. In the context of the LES with smooth walls here,
 496 z_{0m}^{mic} is given by the wall-model (Eq. 3) and also depends on u_* . If we substitute the wall-model into equation B 1, the
 resulting wall-modeled scalar flux F_s follows

$$497 F_s \propto \left(\frac{9}{\kappa}\right)^{1/4} S_c^{-1/2} u_*^{wm} (\theta_s - \theta_h), \quad (B 2)$$

498 where $S_c = \nu/D_m$ is the molecular Schmidt number; θ_h is the mean scalar magnitude in the vicinity of the surface.

By virtue of the wall model here, where $S_c=1$, Eq. B 2 becomes

$$499 F_s \propto u_*^{wm} (\theta_s - \theta_h). \quad (B 3)$$

500 Figure B 1 shows F_s versus u_*^{wm} and the least-square regression using u_*^{wm} computed from all facets for all cases in
 501 Table 1. The data from LES suggest that F_s practically follows a linear scaling with u_*^{wm} , (i.e. the power exponent
 502 is $1.005 \approx 1.0$), which confirms that imposing a smooth-surface micro-scale roughness length in the wall model for
 503 LES is consistent with the prediction in Eq. B 3 and the general surface renewal theory scaling when a smooth-wall
 504 roughness length is desired. In fact, Eq. B 3 or Eq. 11 are more generalizable results since surface renewal theory at
 505 the micro-scale does not need to be invoked to obtain these relations (Katul and Liu, 2017). Imposing a wall function
 in LES based on the log-law formulation implicitly satisfies the assumptions of Kolmogorov's inertial subrange scaling

506 (Gioia et al., 2010). This finding suggests that the results obtained from LES wall-models are not dependent on the
 507 validity of surface renewal theory at the micro-scale. The analysis here is intended to show self-consistency of the
 508 wall-modeling approach adopted here.

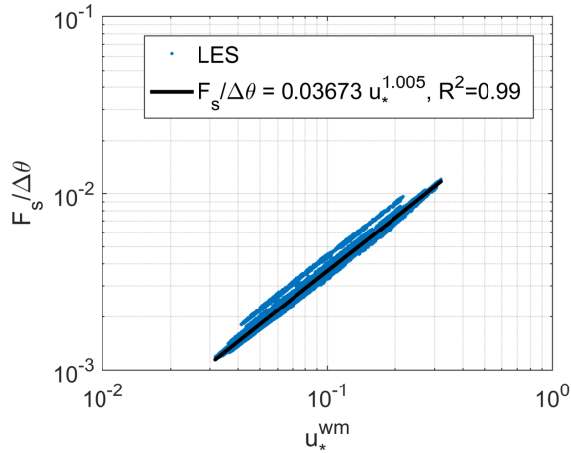


FIGURE B 1 $F_s / (\theta_s - \theta_h)$ versus u_*^{wm} for all LES runs. Each data point represents the mean F_s and u_*^{wm} obtained from the wall model.

509 Appendix C: Uncertainty Analysis in the Delineation of the Log-Region on Macro-Roughness Parameters

510 The delineation of the logarithmic region affects the zero-plane displacement and roughness length estimation is
 511 explored using least-squares regression fitting over all plausible ranges in the logarithmic region (from just above the
 512 building height to three times the building height by visual inspection of the profiles), using at least six points. A
 513 relative sensitivity factor is defined for each fitted parameter Y as $Y - Y_0 / (Y_{max} - Y_{min})$, where Y_0 is the value for the
 514 range of fitting adopted in the paper (i.e. logarithmic region starts from $1.25H$ and ends at $2.25H$); Y is the value of a
 515 given range; $Y_{max} (min)$ is the maximum (minimum) value of Y obtained for all possible ranges. The parameters tested
 516 are z_{0m} , z_{0s} or d , and their sensitivity plots are shown in Fig.C 1, Fig.C 2 and Fig. C 3, respectively.

517 The relative sensitivity factor, D_v , averaged for each geometry over all plausible ranges of the log-region in which
 518 the least-square fitting is performed, is always less than about 40%, and it is within 20% for most of the cases (Fig. C 4).
 519 Therefore, the sensitivity of results to the precise delineation of the logarithmic regions does not change the overall
 520 trends in $B^{-1} = \log(z_{0m}/z_{0s})$ as shown in Fig. C 5). The conclusions of the paper are deemed robust to uncertainties
 521 in the identification of the log-region.

522 references

- 523 Anderson, W. (2013) Passive scalar roughness lengths for atmospheric boundary layer flow over complex, fractal topographies.
 524 *Environmental Fluid Mechanics*, **13**, 479–501.
- 525 Barlow, J. F. and Coceal, O. (2009) A review of urban roughness sublayer turbulence. *Met Office Research and Development–*
 526 *Technical Report*, **1**, 527.

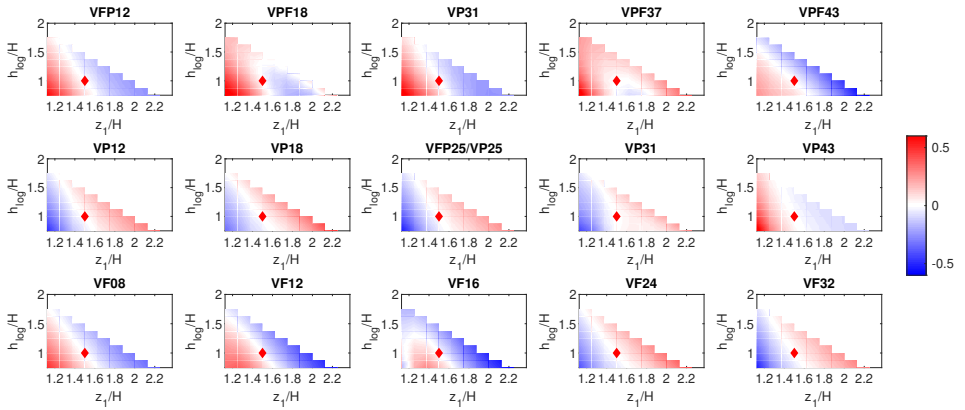


FIGURE C 1 The range of variability of z_{0m} obtained by varying z_1/H , the position where the log-layer commences, and the span of the log-region, h_{log}/H . The red diamond shape denotes the chosen range of the log-region for least-square regression featured in the main text (i.e. $z_1/H = 1.25$ and $h_{log}/H = 1$). Colorbar indicates the relative sensitivity factor.

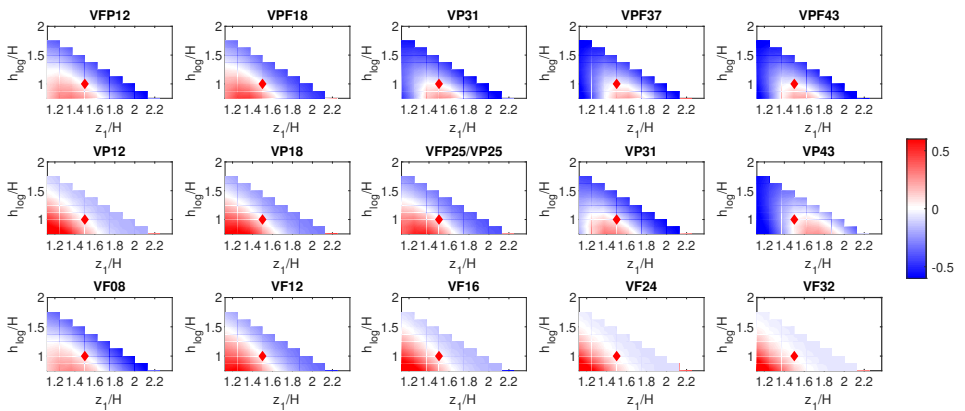


FIGURE C 2 As Fig.C1 , but for z_{0s} .

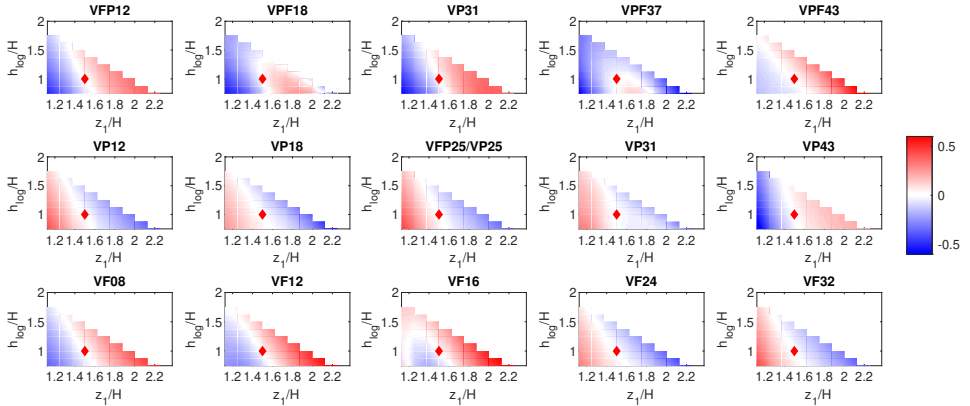


FIGURE C 3 As Fig.C1, but for d .

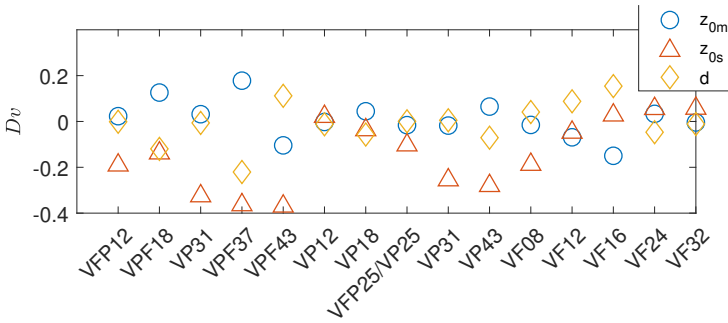


FIGURE C 4 Averaged sensitivity factor Dv for z_{0m} , z_{0s} and d .

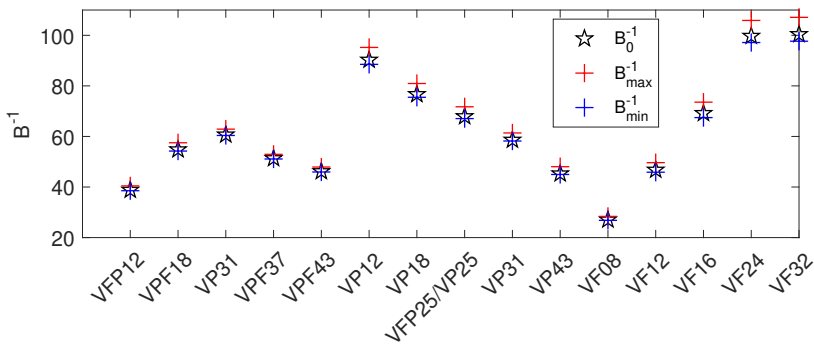


FIGURE C 5 Variation of B^{-1} across cases. B_0^{-1} is computed from z_{0m} and z_{0s} obtained for $z_1/H = 1.25$ and $h_{log}/H = 1$; B_{max}^{-1} and B_{min}^{-1} are obtained from the maximum and minimum values of z_{0m}/z_{0s} for all values from the possible ranges of logarithmic region.

- 527 Barlow, J. F., Harman, I. N. and Belcher, S. E. (2004) Scalar fluxes from urban street canyons. Part I: Laboratory simulation.
528 *Boundary-Layer Meteorology*, **113**, 369–385.
- 529 Bose, S. T. and Park, G. I. (2018) Wall-modeled large-eddy simulation for complex turbulent flows. *Annual Review of Fluid*
530 *Mechanics*, **50**, 535–561.
- 531 Bou-Zeid, E., Meneveau, C. and Parlange, M. (2005) A scale-dependent Lagrangian dynamic model for large eddy simulation
532 of complex turbulent flows. *Physics of Fluids*, **17**, 1–18.
- 533 Bou-Zeid, E., Overney, J., Rogers, B. D. and Parlange, M. B. (2009) The effects of building representation and clustering in
534 large-eddy simulations of flows in urban canopies. *Boundary-Layer Meteorology*, **132**, 415–436.
- 535 Brutsaert, W. (1965) A model for evaporation as a molecular diffusion process into a turbulent atmosphere. *Journal of Geo-*
536 *physical Research*, **70**, 5017.
- 537 – (1975a) A theory for local evaporation (or heat transfer) from rough and smooth surfaces at ground level. *Water Resources*
538 *Research*, **11**, 543–550.
- 539 – (1975b) The roughness length for water vapor sensible heat, and other scalars. *Journal of Atmospheric Sciences*, **32**, 2028–
540 2031.
- 541 – (1982) *Evaporation into the atmosphere: theory, history and applications*, vol. 1. Springer Science & Business Media.
- 542 Cai, X.-M. (2012) Effects of wall heating on flow characteristics in a street canyon. *Boundary-Layer Meteorology*, **142**, 443–467.
- 543 Castellví, F. (2018) An advanced method based on surface renewal theory to estimate the friction velocity and the surface
544 heat flux. *Water Resources Research*, **54**, 10–134.
- 545 Castellvi, F., Snyder, R. and Baldocchi, D. (2008) Surface energy-balance closure over rangeland grass using the eddy covari-
546 ance method and surface renewal analysis. *Agricultural and Forest Meteorology*, **148**, 1147–1160.
- 547 Chen, F. and Zhang, Y. (2009) On the coupling strength between the land surface and the atmosphere: From viewpoint of
548 surface exchange coefficients. *Geophysical Research Letters*, **36**.
- 549 Chen, Y., Yang, K., Zhou, D., Qin, J. and Guo, X. (2010) Improving the noah land surface model in arid regions with an appro-
550 priate parameterization of the thermal roughness length. *Journal of Hydrometeorology*, **11**, 995–1006.
- 551 Chester, S., Meneveau, C. and Parlange, M. B. (2007) Modeling turbulent flow over fractal trees with renormalized numerical
552 simulation. *Journal of Computational Physics*, **225**, 427–448.
- 553 Chung, J., Hagishima, A., Ikegaya, N. and Tanimoto, J. (2015) Wind-Tunnel Study of Scalar Transfer Phenomena for Surfaces
554 of Block Arrays and Smooth Walls with Dry Patches. *Boundary-Layer Meteorology*, **157**, 219–236.
- 555 Clayton, C. A., Fairall, C. W. and Curry, J. A. (1996) Evaluation of turbulent fluxes at the ocean surface using surface renewal
556 theory. *Journal of Geophysical Research: Oceans*, **101**, 28503.
- 557 Crawford, B., Grimmond, S. B., Gabey, A., Marconcini, M., Ward, H. C. and Kent, C. W. (2018) Variability of urban surface
558 temperatures and implications for aerodynamic energy exchange in unstable conditions. *Quarterly Journal of the Royal*
559 *Meteorological Society*, **144**, 1719–1741.
- 560 Danckwerts, P. V. (1951) Significance of liquid-film coefficients in gas absorption. *Industrial & Engineering Chemistry*, **43**, 1460–
561 1467.
- 562 De Ridder, K. (2006) Testing brutsaert's temperature roughness parameterization for representing urban surfaces in atmo-
563 spheric models. *Geophysical Research Letters*, **33**.

- 564 Demuzere, M., De Ridder, K. and Van Lipzig, N. (2008) Modeling the energy balance in marseille: Sensitivity to roughness
565 length parameterizations and thermal admittance. *Journal of Geophysical Research: Atmospheres*, **113**.
- 566 Denby, B. and Snellen, H. (2002) A comparison of surface renewal theory with the observed roughness length for temperature
567 on a melting glacier surface. *Boundary-Layer Meteorology*, **103**, 459–468.
- 568 Flack, K. A. and Schultz, M. P. (2014) Roughness effects on wall-bounded turbulent flows. *Physics of Fluids*, **26**.
- 569 Fowler, A. J. and Bejan, A. (1995) Forced convection from a surface covered with flexible fibers. *International journal of heat
570 and mass transfer*, **38**, 767–777.
- 571 Garratt, J. (1980) Surface influence upon vertical profiles in the atmospheric near-surface layer. *Quarterly Journal of the Royal
572 Meteorological Society*, **106**, 803–819.
- 573 Garratt, J. R. (1992) The atmospheric boundary layer, cambridge atmos. *Space Sci. Ser., Cambridge Univ. Press, Cambridge, UK*.
- 574 Ghisalberti, M. (2009) Obstructed shear flows: similarities across systems and scales. *Journal of Fluid Mechanics*, **641**, 51–61.
- 575 Gioia, G., Guttenberg, N., Goldenfeld, N. and Chakraborty, P. (2010) Spectral theory of the turbulent mean-velocity profile.
576 *Physical review letters*, **105**, 184501.
- 577 Giometto, M. G., Christen, A., Meneveau, C., Fang, J., Krafczyk, M. and Parlange, M. B. (2016) Spatial Characteristics of
578 Roughness Sublayer Mean Flow and Turbulence Over a Realistic Urban Surface. *Boundary-Layer Meteorology*, 1–28.
- 579 Grimmond, C. and Oke, T. R. (1999) Aerodynamic properties of urban areas derived from analysis of surface form. *Journal of
580 Applied Meteorology*.
- 581 – (2002) Turbulent heat fluxes in urban areas: Observations and a local-scale urban meteorological parameterization scheme
582 (lumps). *Journal of Applied Meteorology*, **41**, 792–810.
- 583 Hagishima, A., Tanimoto, J., Nagayama, K. and Meno, S. (2009) Aerodynamic parameters of regular arrays of rectangular blocks
584 with various geometries. *Boundary-Layer Meteorology*, **132**, 315–337.
- 585 Harman, I. N. and Finnigan, J. J. (2007) A simple unified theory for flow in the canopy and roughness sublayer. *Boundary-Layer
586 Meteorology*, **123**, 339–363.
- 587 – (2008) Scalar concentration profiles in the canopy and roughness sublayer. *Boundary-Layer Meteorology*, **129**, 323–351.
- 588 Ikegaya, N., Hagishima, A., Tanimoto, J., Tanaka, Y., Narita, K. and Zaki, S. A. (2012) Geometric Dependence of the Scalar
589 Transfer Efficiency over Rough Surfaces. *Boundary-Layer Meteorology*, **143**, 357–377.
- 590 Jackson, P. S. (1981) On the displacement height in the logarithmic velocity profile. *Journal of Fluid Mechanics*, **111**, 15.
- 591 Kader, B. and Yaglom, A. (1972) Heat and mass transfer laws for fully turbulent wall flows. *International Journal of Heat and
592 Mass Transfer*, **15**, 2329–2351.
- 593 Kanda, M., Inagaki, A., Miyamoto, T., Gryschka, M. and Raasch, S. (2013) A new aerodynamic parametrization for real urban
594 surfaces. *Boundary-Layer Meteorology*, **148**, 357–377.
- 595 Kanda, M., Kanega, M., Kawai, T., Moriwaki, R. and Sugawara, H. (2007) Roughness lengths for momentum and heat derived
596 from outdoor urban scale models. *Journal of Applied Meteorology and Climatology*, **46**, 1067–1079.
- 597 Kanda, M., Moriwaki, R. and Kasamatsu, F. (2004) Large-eddy simulation of turbulent organized structures within and above
598 explicitly resolved cube arrays. *Boundary-Layer Meteorology*, **112**, 343–368.
- 599 Kastner-Klein, P. and Rotach, M. W. (2004) Mean Flow and Turbulence Characteristics in an Urban Roughness Sublayer.
600 *Boundary-Layer Meteorology*, **111**, 55.

- 601 Katul, G., Geron, C., Hsieh, C., Vidakovic, B. and Guenther, A. (1998) Active turbulence and scalar transport near the forest-
602 atmosphere interface. *Journal of Applied Meteorology*, **37**, 1533–1546.
- 603 Katul, G., Hsieh, C.-I., Oren, R., Ellsworth, D. and Phillips, N. (1996) Latent and sensible heat flux predictions from a uniform
604 pine forest using surface renewal and flux variance methods. *Boundary-Layer Meteorology*, **80**, 249–282.
- 605 Katul, G. and Liu, H. (2017) A kolmogorov-brutsaert structure function model for evaporation into a turbulent atmosphere.
606 *Water Resources Research*, **53**, 3635–3644.
- 607 Katul, G., Porporato, A., Cava, D. and Siqueira, M. (2006) An analysis of intermittency, scaling, and surface renewal in atmo-
608 spheric surface layer turbulence. *Physica D: Nonlinear Phenomena*, **215**, 117–126.
- 609 Kent, C. W., Grimmond, C., Barlow, J., Gatey, D., Kotthaus, S., Lindberg, F. and Halios, C. H. (2017) Evaluation of Urban Local-
610 Scale Aerodynamic Parameters: Implications for the Vertical Profile of Wind Speed and for Source Areas. *Boundary-Layer
611 Meteorology*, **164**, 1–31.
- 612 Leonardi, S. and Castro, I. P. (2010) Channel flow over large cube roughness: a direct numerical simulation study. *Journal of
613 Fluid Mechanics*, **651**, 519.
- 614 Leonardi, S., Orlandi, P., Djenidi, L. and Antonia, R. A. (2015) Heat transfer in a turbulent channel flow with square bars or
615 circular rods on one wall. *Journal of Fluid Mechanics*, **776**, 512–530.
- 616 Lhomme, J.-P. (1991) The concept of canopy resistance: historical survey and comparison of different approaches. *Agricultural
617 and forest Meteorology*, **54**, 227–240.
- 618 Li, D. and Bou-Zeid, E. (2014) Quality and sensitivity of high-resolution numerical simulation of urban heat islands. *Environ-
619 mental Research Letters*, **9**, 055001.
- 620 Li, D., Rigden, A., Salvucci, G. and Liu, H. (2017) Reconciling the Reynolds number dependence of scalar roughness length and
621 laminar resistance. *Geophysical Research Letters*, **44**, 3193–3200.
- 622 Li, Q. and Bou-Zeid, E. (2019) Contrasts between momentum and scalar transport over very rough surfaces. *Journal of Fluid
623 Mechanics*, **880**, 32–58.
- 624 Li, Q., Bou-Zeid, E. and Anderson, W. (2016a) The impact and treatment of the Gibbs phenomenon in immersed boundary
625 method simulations of momentum and scalar transport. *Journal of Computational Physics*, **310**, 237–251.
- 626 Li, Q., Bou-Zeid, E., Anderson, W., Grimmond, C. and Hultmark, M. (2016b) Quality and reliability of les of convective scalar
627 transfer at high reynolds numbers. *International Journal of Heat and Mass Transfer*, **102**, 959–970.
- 628 Li, Q., Bou-Zeid, E., Vercauteren, N. and Parlange, M. B. (2018) Signatures of air-wave interactions over a large lake. *Boundary-
629 Layer Meteorology*, **167**, 445–468.
- 630 Llaguno-Munitxa, M. and Bou-Zeid, E. (2018) Shaping buildings to promote street ventilation: A large-eddy simulation study.
631 *Urban climate*, **26**, 76–94.
- 632 Macdonald, R. W., Griffiths, R. F. and Hall, D. J. (1998) An improved method for the estimation of surface roughness of obstacle
633 arrays. *Atmospheric Environment*, **32**, 1857–1864.
- 634 Masson, V. (2000) A physically-based scheme for the urban energy budget in atmospheric models. *Boundary-Layer Meteorology*,
635 **94**, 357–397.
- 636 Monin, A. S. and Obukhov, A. M. (1954) Osnovnye zakonomernosti turbulentnogo peremesivaniya v prizemnom sloe atmosfery.
637 *Trudy Geofiz. Inst. AN SSSR*, **24**, 163–187.
- 638 Moog, D. and Jirka, G. (1999) Air-water gas transfer in uniform channel flow. *Journal of Hydraulic Engineering*, **125**, 3–10.

- 639 Moriwaki, R. and Kanda, M. (2006a) Scalar Roughness Parameters for a Suburban Area. *Journal of the Meteorological Society*
640 *of Japan*, **84**, 1063.
- 641 – (2006b) Scalar roughness parameters for a suburban area. *Journal of the Meteorological Society of Japan. Ser. II*, **84**, 1063–
642 1071.
- 643 Morrison, W., Yin, T., Lauret, N., Guilleux, J., Kotthaus, S., Gastellu-Etchegorry, J.-P., Norford, L. and Grimmond, S. (2020)
644 Atmospheric and emissivity corrections for ground-based thermography using 3d radiative transfer modelling. *Remote*
645 *Sensing of Environment*, **237**, 111524.
- 646 Nikuradse, J. (1933) Laws of Flow in Rough Pipes - Translation of "Stromungsgesetze in rauhen Rohren". *Tech. rep.*
- 647 Owen, P. R. and Thomson, W. (1963) Heat transfer across rough surfaces. *Journal of Fluid Mechanics*, **15**, 321–334.
- 648 Perry, A. E., Schofield, W. H. and Joubert, P. N. (1969) Rough wall turbulent boundary layers. *Journal of Fluid Mechanics*, **37**,
649 383–413.
- 650 Placidi, M. and Ganapathisubramani, B. (2015) Effects of frontal and plan solidities on aerodynamic parameters and the rough-
651 ness sublayer in turbulent boundary layers. *Journal of Fluid Mechanics*, **782**, 541–566.
- 652 Poggi, D., Porporato, A., Ridolfi, L., Albertson, J. and Katul, G. (2004) The effect of vegetation density on canopy sub-layer
653 turbulence. *Boundary-Layer Meteorology*, **111**, 565–587.
- 654 Pope, S. B. (2000) *Turbulent flows*. Cambridge: Cambridge University Press.
- 655 Raupach, M. R., Finnigan, J. J. and Brunei, Y. (1996) Coherent eddies and turbulence in vegetation canopies: The mixing-layer
656 analogy. *Boundary-Layer Meteorology*, **78**, 351–382.
- 657 Ryu, Y. H., Baik, J. J. and Lee, S. H. (2011) A new single-layer urban canopy model for use in mesoscale atmospheric models.
658 *Journal of Applied Meteorology and Climatology*, **46**, 1067–1079.
- 659 Schmugge, T., Kustas, W., Ritchie, J., Jackson, T. and Rango, A. (2002) Remote sensing in hydrology. *Advances in Water*
660 *Resources*, **25**, 1367–1385.
- 661 Siqueira, M. B. and Katul, G. G. (2010) An analytical model for the distribution of co₂ sources and sinks, fluxes, and mean
662 concentration within the roughness sub-layer. *Boundary-Layer Meteorology*, **135**, 31–50.
- 663 Slotnick, J., Khodadoust, A., Alonso, J., Darmofal, D., Gropp, W., Lurie, E. and Mavriplis, D. (2014) Cfd vision 2030 study: a
664 path to revolutionary computational aerosciences. *NASA Tech. Rep. CR-2014-218178*, Langley Res. Cent., Hampton, VA.
- 665 Snyder, R., Spano, D. and Pawu, K. (1996) Surface renewal analysis for sensible and latent heat flux density. *Boundary-Layer*
666 *Meteorology*, **77**, 249–266.
- 667 Sullivan, P. P., Banner, M. L., Morison, R. P. and Peirson, W. L. (2017) Turbulent Flow over Steep Steady and Unsteady Waves
668 under Strong Wind Forcing. *Journal of Physical Oceanography*, **48**, 3–27.
- 669 Theeuwes, N. E., Ronda, R. J., Harman, I. N., Christen, A. and Grimmond, C. S. B. (2019) Parametrizing horizontally-averaged
670 wind and temperature profiles in the urban roughness sublayer. *Boundary-Layer Meteorology*, **173**, 321–348.
- 671 Tseng, Y. H., Meneveau, C. and Parlange, M. B. (2006) Modeling flow around bluff bodies and predicting urban dispersion
672 using large eddy simulation. *Environmental Science & Technology*, **40**, 2653–2662.
- 673 Voogt, J. A. and Grimmond, C. S. B. (2000) Modeling Surface Sensible Heat Flux Using Surface Radiative Temperatures in a
674 Simple Urban Area. *Journal of Applied Meteorology*, **39**, 1679.
- 675 Wang, Z.-H., Bou-Zeid, E. and Smith, J. A. (2013) A coupled energy transport and hydrological model for urban canopies
676 evaluated using a wireless sensor network. *Quarterly Journal of the Royal Meteorological Society*, **139**, 1643–1657.

- 677 Yang, X., Hu, H., Huang, X. and Ge, M. (2019) Drag forces on sparsely packed cube arrays. *Journal of Fluid Mechanics*.
- 678 Yang, X. I. and Abkar, M. (2018) A hierarchical random additive model for passive scalars in wall-bounded flows at high
679 Reynolds numbers. *Journal of Fluid Mechanics*.
- 680 Yang, X. I. A., Sadique, J., Mittal, R. and Meneveau, C. (2016) Exponential roughness layer and analytical model for turbulent
681 boundary layer flow over rectangular-prism roughness elements. *Journal of Fluid Mechanics*, **789**, 127.
- 682 Zhu, X. and Anderson, W. (2018) Turbulent flow over urban-like fractals: prognostic roughness model for unresolved genera-
683 tions. *Journal of Turbulence*, **19**, 995–1016.
- 684 Zhu, X., Iungo, G. V., Leonardi, S. and Anderson, W. (2017) Parametric study of urban-like topographic statistical moments
685 relevant to a priori modelling of bulk aerodynamic parameters. *Boundary-Layer Meteorology*, **162**, 231–253.
- 686 Zilitinkevich, S. S., Grachev, A. A. and Fairall, C. W. (2001) Notes and correspondence: Scaling reasoning and field data on the
687 sea surface roughness lengths for scalars. *Journal of the Atmospheric Sciences*, **58**, 320–325.